Planetary transit candidates observed by ASTEP 400

D. Mékarnia[1] *, T. Guillot[1], I. Gonçalves[1], L. Abe[1], A. Agabi[1], J.-P. Rivet[1],
F.-X. Schmider[1], N. Crouzet[2], D.D.R. Bayliss[3], G. Zhou[3], E. Aristidi[1], J.-B. Daban[1],
Y. Fanteï-Caujolle[1], C. Gouvret[1], J. Szulagyi[1], T. Fruth[4], A. Erikson[4], H. Rauer[4],
F. Bouchy[5], J. Gérakis[1] and G. Bouchez[6]

[1] *Laboratoire Lagrange, UMR 7293, Université de Nice Sophia-Antipolis, CNRS, Observatoire de la Côte d'Azur, BP 4229, F-06304 Nice Cedex 4, France.*
[2] *Dunlap Institute for Astronomy & Astrophysics, University of Toronto, 50 St. George Street, Toronto, Ontario M5S 3H4, Canada.*
[3] *Research School of Astronomy and Astrophysics, Australian National University, Canberra, ACT 2611, Australia.*
[5] *Aix Marseille Université, CNRS, LAM (Laboratoire dAstrophysique de Marseille) UMR 7326, F-13388 Marseille, France.*
[6] *GEMAC, Université de Versailles, CNRS, 45 av. des Etats-Unis, 78035 Versailles Cedex, France.*

ABSTRACT
ASTEP 400, which is the main instrument of the ASTEP (Antarctica Search for Transiting ExoPlanets) program, is a 40 cm telescope, designed to withstand the harsh conditions in Antarctica, achieving a photometric accuracy of a fraction of milli-magnitude. We review the performances of this instrument, describe its operating conditions, its performances and present results from the analysis of observations obtained during the first three years (2010-2012) of operation of the instrument. During this period, we observed a total of 21 stellar fields (1º×1º FoV). Each field, containing stars at magnitudes up to R=18 mag, was observed continuously during ~7 to ~30 days. More than 200 000 frames were recorded and 310 000 stars analysed. Data were processed using an implementation of the optimal image subtraction (OIS) algorithm. We found 43 possible planetary transit candidates and more than 1 900 new variables stars. Twenty of these candidates were observed using spectroscopic follow-up. Five planetary candidates present no RV variations within $2 \, \mathrm{km \, s^{-1}}$ level for which higher spectroscopic resolution observations are needed. Two candidates present no RV variations within $5 \, \mathrm{km \, s^{-1}}$ level for which more accurate followed-up are required to confirm their possible planetary status. We present here all of these candidates along with their detailed properties derived from transit observations as well as from follow-up observations. Our results demonstrate that extremely stable and precise visible photometry and near-continuous observations are achievable from the Concordia station at Dome C in Antarctica.

Key words: Instrumentation: photometers – methods: data analysis – methods: observational – stars: – (stars:) planetary systems

1 INTRODUCTION

Dome C, on the East Antarctic plateau, is one of the most promising sites for visible, infrared and sub millimeter astronomy. An extensive range of wintertime measurements of the atmospheric turbulence have been made over this site revealing a very low cloud cover sky, an exceptional seeing above a thin boundary layer, very low wind-speeds (Aristidi et al. 2003, 2005, 2009; Lawrence et al. 2004; Fossat et al. 2010; Giordano et al. 2012), a very low scintillation noise leading to superior photometric precision measurements (Kenyon et al. 2006), a high duty cycle

(Mosser & Aristidi 2007; Moore et al. 2008; Crouzet et al. 2010) and a low sky brightness and extinction (Kenyon & Storey 2006). Optical photometry from Dome C were highlighted by several authors (Kenyon et al. 2006; Strassmeier et al. 2008; Crouzet et al. 2013; Abe et al. 2013). Dome A, another promising site on the Antarctic plateau, may provide such very favorable conditions (Bonner et al. 2010; Wang et al. 2011). Furthermore, polar sites have the following obvious advantages leading to perform long, continuous time-series observations: *i*) a quasi-continuous astronomical darkness for about 4 months, for instruments exploiting the visible and NIR spectral bands, longer wavelengths being observed continuously year-round, and *ii*) a little changes in the elevation of the observed sources.
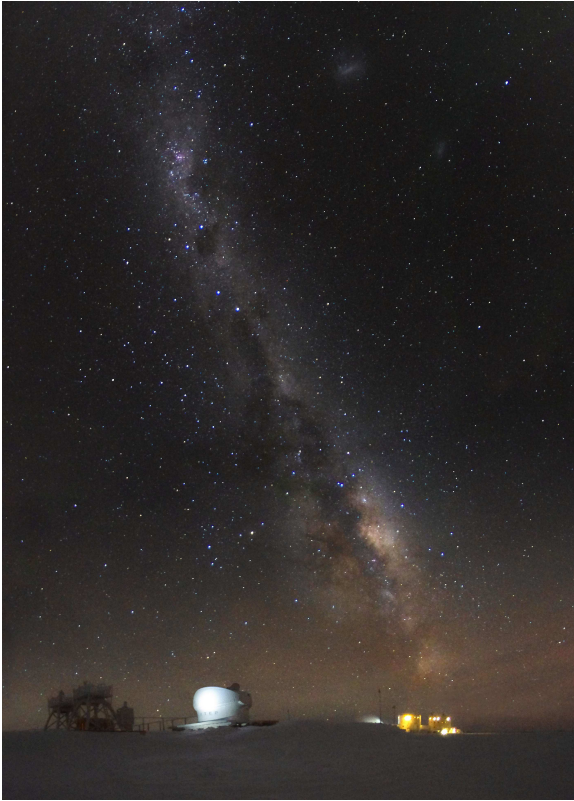
* E-mail: mekarnia@oca.eu

Figure 1. ASTEP 400 operating at Concordia Station (Dome C, Antarctica), during the 2011 winter. Image courtesy of E. MacDonald.

The ASTEP program (Antarctic Search for Transiting Exo-Planets) comprises two instruments: ASTEP South, a fixed 10 cm, 3.9°×3.9° field of view refractor pointed towards the celestial South Pole (Crouzet et al. 2010), and the ASTEP 400 telescope, a 40 cm Newton reflector with a 1°×1° field of view. Both instruments are dedicated to finding and characterizing transiting exoplanets, although the ASTEP South, as a precursor, was mainly used to probe the photometric capabilities of the site (Crouzet et al. 2010). These instruments use facilities provided by the French-Italian Antarctic station Concordia, located at Dome C (75°06'S, 123°21'E) at an altitude of 3233 m, 1100 km inland from the nearest coast. ASTEP South was installed in 2008 whereas ASTEP 400, subject of this paper, was installed in December 2009 and has operated from 2010 to 2013.

We present here the ASTEP 400 instrument and the exoplanetary transit candidates resulting from analysis of the 2010-2012 Antarctic winter seasons. We first review the characteristics of the instrument, its performances, and describe its operating conditions as well as the observation strategy. Section 3 describes the data processing, the steps followed to perform high-precision time-series photometry and the noise analysis. In Section 4 we present the transit searching method and the follow-up observations of a sample of our exoplanetary transit candidates. We report some properties for each transit candidate in Section 5 and summarized the work in Section 6.

2 INSTRUMENTATION AND OBSERVATIONS

2.1 Instrumental set up

ASTEP 400 is a custom 40 cm Newtonian telescope with a sophisticated field corrector, designed to withstand both Dome C summer and winter temperatures ranging from -20°C to -80°C with rapid variations. The primary mirror diameter is 40 cm with a focal ratio of 4.6 (Fig. 1). Because of its wide field of view (1°×1°) and of the layout of the optics and cameras in the focal box, the secondary mirror is quite big giving a central obstruction of 42% of the primary mirror. Both primary and secondary mirrors are made in glass ceramic material ZERODUR and coated with aluminium. Even if a better transmission is provided with silver coatings we choose aluminium because of its very good resistance to the Antarctic environment, and because we do not have any experience with silver coatings in such harsh climatic conditions. To achieve a good thermal and mechanical stability, the mechanical structure of the telescope is a 8-th order Serrurier truss with carbon fiber legs, connected to an aluminium alloy main frame through Invar^{TM} sleeves (Fig. 2). The telescope structure is covered by a two-layer envelope to protect optics both against stray lights and ice dust deposit. Finite element analysis was carried out to predict the deformations of the structure as a function of the telescope positions and temperature variations and their impact on the PSF quality and stability. Even with this careful design and manufacturing, the thermal expansion during rapid temperature variations may yield a telescope defocus of ~150 μm for a gradient temperature of 30°C.

The telescope and the focal box camera were designed, developed and constructed by our team while the telescope mount is a commercial equatorial AP 3600 from Astro-Physics Inc. that we adapted to the harsh Antarctic conditions (i.e. by changing the grease, heating the drive motors and by making a slight mechanical adaptation of few components). Since the telescope is observing almost continuously, the mount is re-winded automatically, when it exceeds 2 or 3 spins, to prevent winding of the connection cables.

Figure 3 illustrates the design of the focal box, which is divided into two compartments. The first compartment contains only optical components, dichroic plate (D) and M3 mirror, while the second compartment contains the "Science" and "Guiding" cameras, the motorized translation stage and their electronics. The focal box receives the incoming beam from the Newtonian telescope's flat secondary mirror through the two first lenses of the 5-lens Wynne coma corrector, which act as a double-glazed insulation window. These lenses, along with the three other lenses located between the dichroic mirror and the Science camera, contribute to the field correction yielding an excellent image quality over the 1° × 1° FoV.

The focal box is mounted on a carbon fiber plate ensuring its rigidity and thermal stability. The opto-mechanical mounts are in titanium alloy which is a good choice in terms of weight, strength and thermal expansion coefficient. The dichroic mirror (D) separates the Science path from the telescope guiding path. The red part of the spectrum ($\lambda > 0.6\,\mu$m) leads to the Science camera while the blue part ($\lambda < 0.6\,\mu$m) leads to the Guiding camera. The Science camera is an FLI Proline with a KAF 16801E, 4096 × 4096 pixels front-illuminated CCD with a 16 bits analog to digital converter. The CCD dimension is 36.8 mm × 36.8 mm and the plate scale is 0.92" per pixel (1 pixel = 9 μm). The Science camera, which is cooled by a Peltier device, is mounted on a remote controlled translation stage, which adjusts the telescope focal position within 5 μm accuracy. The camera is slightly defocused to spread the Point Spread Function (PSF) Full Width at Half-Maximum (FWHM) to

about 3 pixels reducing the jitters noise due to the inter-pixel and extra-pixel inhomogeneity. The camera can be removed and replaced with He-Ne laser for the optical alignment of the whole instrument. The PSF is stable and homogeneous from the center to the corner of the CCD, with a FWHM below 3 pixels when atmospheric turbulence is low and stable. This is not always the case because the entrance telescope pupil is at about 2 m above the ice surface, which is far from optimal seeing conditions at Dome C. The Guiding camera is a SBIG ST402M ensuring, in normal observing conditions, a resulting guiding accuracy of about 0.2" RMS or better.

Electronic components of the focal box cannot withstand the very low Antarctic temperatures. Consequently, the two compartments of the focal box were insulated using both cellular polystyrene plates (Depron^{TM}), which stem heat conduction, and reflective layers (Kapton^{TM}), to prevent heat radiation. The two compartments were heated with electric resistors to maintain their surrounding at temperatures compatible with safe operations. PT 100 thermometer probes are used to give feedback on regulators. The first compartment is stabilized at around -40°C, while the second compartment is held at approximately -10°C. On the other hand the Science camera front panel is held at $+5^{o}$C as the FLI mechanical shutter cannot operate at lower temperatures. All the thermal controllers are linked via a RS 485 bus to the main control computer through a RS 485/RS 232 adapter. So, all component temperatures can be monitored, and the set points of the controllers adjusted by software.

The double-glazed optical window of the focal box, composed of the two first meniscus lenses of the Wynne field corrector, minimizes heat loss, and consequently prevents turbulence in the optical path of the instrument. Lenses of the Wynne field corrector are in fused silica in order to minimize their thermo-elastic deformations. Moreover, insulation of the focal box guaranties a long life of the dichroic coating when external temperature can reach -80°C in winter.

2.2 Control software

The telescope is driven by a custom made software, designed to operate both in a manual, or a so-called automatic mode of operation. In the latter mode, a custom script describing a set of independent observing fields feeds the software. Each field has its own observational constraints (priority, temporal boundaries, sun elevation, periodicity...) so the software schedules the observation of each field following these constraints. To ensure proper pointing of the telescope in the automatic mode, the software uses a built-in field recognition algorithm capable of re-pointing the telescope even in the case where the telescope pointing error is larger than 1°.

ASTEP 400 is connected to a dedicated computing and mass storage server (32 CPUs, ~20 TiB). Data are locally stored onto a data acquisition PC (2 TiB disk capacity) and backed up automatically, every day, on the mass storage. A second data backup is made on TiB-capacity hard drives and sent back to France during the summer campaign. A data backup hard drives set is kept on-site for security in the (rare) cases of disk failures or shipping problems.

2.3 Frosting and snow deposit

During Antarctic winter the temperature, which can fall to -80°C, is characterized by some rapid variations that can reach several degrees. In such conditions, the relative humidity leads to ice nucleation and frost formation on the primary mirror of the telescope,
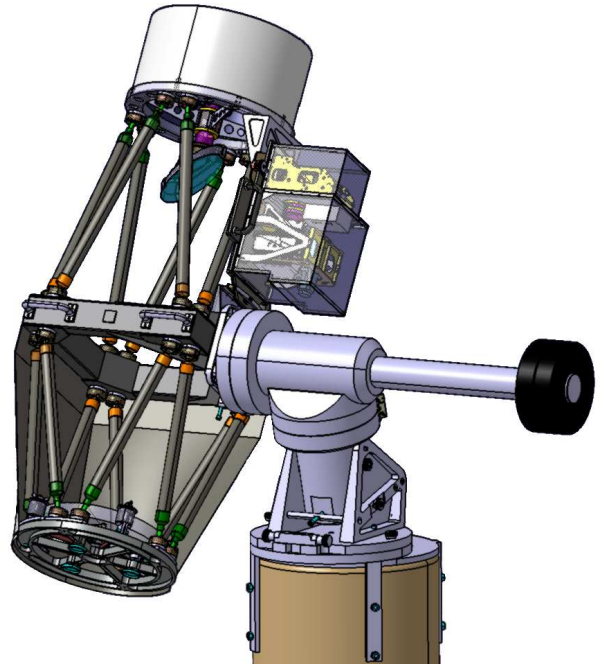
Figure 2. Engineering model of ASTEP 400. The mechanical structure of the telescope is an 8-th order Serrurier truss. The main frame in the middle of the structure and both its upper (the secondary mirror spider assembly), and lower part (the primary mirror barrel assembly) are made of aluminium. The hollow bars that link these three parts are made of carbon fiber with Invar^{TM}sleeves at each end. The telescope mount is a commercial equatorial AP3600 from Astro-Physics Inc. that we have adapted to withstand the harsh Antarctic conditions.

and, at lower amount, on the secondary one. Ice dust can also fall on the primary mirror of the telescope. There are two ways to prevent the frost formation and/or snow deposit: *i)* blowing dry air (continuously or from time to time) on optical surfaces or *ii)* warming up them. The first method is useful because it cannot introduce any undesirable turbulence in the optical path of the instrument, whereas the second method is more efficient if temperature gradient does not exceed a few degrees (less then ~6°C and ~2°C for the primary and secondary mirror, respectively).

No defrosting system was originally installed on ASTEP 400. However, during the first season of operation (2010) daily interventions were needed to check the status of the telescope mirrors and occasionally defrost the primary mirror and/or remove the ice dust deposit with a soft brush. To reduce these human interventions as much as possible, we installed, during the 2010-2011-summer campaign, a defrosting setup for both the primary and secondary mirrors. This system consists in a custom designed film resistor attached to the rear surface of each mirror. Temperature probes were glued on the side of these mirrors, and a pair of additional temperature controllers was added to drive the heaters. These new controllers were connected with the other temperature controllers. So, the temperatures of the mirrors can be monitored easily, and the power supplied to the heaters adjusted to avoid any additional optical turbulence caused by this system. To evaluate the defrosting system efficiency, we analysed PSFs as function of temperature gradients of the mirrors. We identified visually that alterations of the PSF quality remained small when the temperature difference between the primary and secondary mirrors and the ambient air remained lower than ~10°C and ~4°C, respectively. However, an a
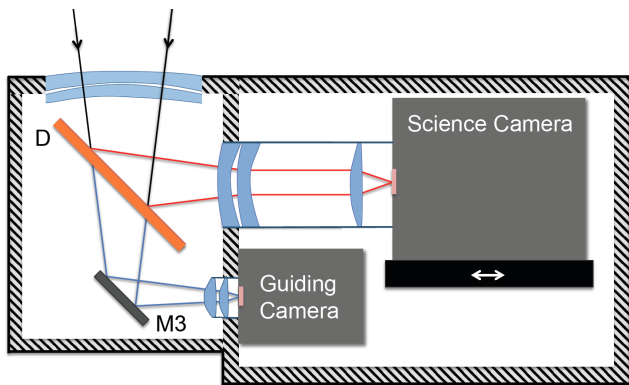
Figure 3. Optical design of the focal box. Light coming from the Newtonian flat's secondary mirror through the double-glazed optical window, is splitted into two beams by the dichroic plate (D) which reflects the red part to the Science camera and transmits the blue part to the Guiding camera through the mirror M3. The two first lenses of the optical window, along with the three other lenses, located between the dichroic plate and the Science camera, contribute to the field coma correction. The Science camera is mounted on a remote controlled translation stage to get the proper focus.
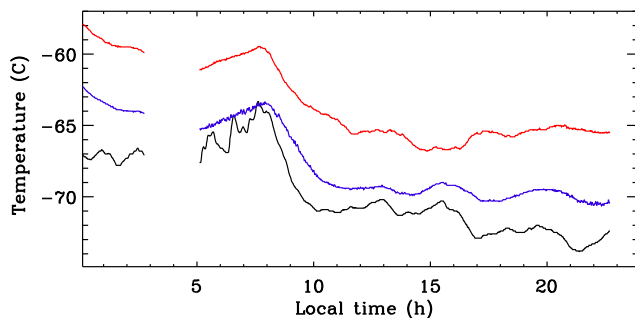

Figure 4. Ambient (black), primary (red) and secondary (blue) temperature mirrors as a function of local time on 4th July 2012. Typical temperature gradients of the primary and secondary mirror are of ~6°C and ~2°C, respectively. Heating up the mirrors in such way prevents frost formation on these mirrors.

posteriori analysis of the data shows that the PSF size increases with the temperature difference, at a rate of $\sim 0.2 \, \Delta T$ " (Guillot et al. 2015. Submitted).

This defrosting setup, installed in 2011, can operate both in "preventive" or "curative" mode. In the preventive mode, a small fraction of the maximum power is supplied to the heaters, so as to maintain the surface mirrors temperature a few degrees above ambient temperature i.e. ~6°C for the primary mirror, and ~2°C for the secondary one (Fig. 4). This mode can run during observations without hampering the PSF quality. Under special weather conditions (rapid increase of the external temperature), some frost can appear in any case or, more frequently, ice dust grains can fall on the optics. Then, the curative mode is activated and 100% of the nominal power of the heaters is supplied, for a short period. This removes the frost and/or ice dust deposit. Of course, no science exposure frames are recorded during this curative phase.

2.4 Observational strategy

ASTEP 400 was designed to achieve photometric accuracy of a fraction of milli-magnitude with a good photometric stability.

These specifications make this instrument ideal for monitoring several thousands of stars to search for transiting exoplanets, and well suited for a variety of wide field imaging and temporal studies, such as discovery and monitoring of variable stars (Mékarnia et al. 2015. In preparation). ASTEP 400 is semi-robotic and fully computer-controlled instrument, so that very few human interventions are required from the winter-over crew. Only regular inspections of the primary and secondary mirrors are needed. Through a single graphic user interface, the winter-over crew member in charge with ASTEP 400 can monitor the relevant parameters of the telescope, perform any modification, send orders to the telescope motor drives, or run pre-determined observation scripts. There are two distinct operational seasons for ASTEP 400 as for any optical instrument located at Dome C: the summer season, from November to end of January, and the winter season, from March to October, with transitional periods (February−March while waiting/preparing for astronomical darkness, and September−October at the end of the winter-over season).

2.4.1 Duty cycle and technical issues

The winter clear sky fraction at Dome C was studied by several authors (Ashley et al. 2005; Mosser & Aristidi 2007; Moore et al. 2008; Crouzet et al. 2010). Mosser & Aristidi (2007) yielded an estimate of 92% of clear sky fraction by reporting several times a day the presence of clouds with the naked eye, Moore et al. (2008) derive a fraction of 79% from the Gattini instrument while Crouzet et al. (2010) and Ashley et al. (2005) found a fraction of 74% from the 2008 ASTEP South data and from the 2001 ICECAM images, respectively. Recently, Petenko et al. (2014) obtained a fraction of 60% of completely clear sky conditions from sodar measurements.

The duty cycle for winter observations at Dome C was qualified by the ASTEP South instrument (Crouzet et al. 2010). The main limitations were related to *i)* the position of the Sun, *ii)* the weather conditions and *iii)* technical issues related to the operation of the instrument. Influence of the Sun (and the Moon) on photometry at Dome C was also studied by Crouzet et al. (2010). It is important to notice that although the Sun is permanently below the horizon from May 6 to August 9, the sky background is always higher around noon making continuous accurate photometric measurements impossible. The R-band sky magnitude at Dome C is 16.6 arcsec^{-2} for a Sun elevation of $-9°$, whilst the sky intensity drops to an undetectable level when the Sun is below $-13°$ (Crouzet et al. 2010). In addition, an increased sky background is clearly seen during periods of full Moon. Therefore, a special attention should be made in the choice of the observed fields during these periods. Aurorae was also feared to be a limit to the long-term photometry in Antarctica, but in any case our data were not contaminated by auroras, confirming that their contribution to the sky brightness at Dome C is negligible, as suggested by Dempsey, Storey & Phillips (2005) and reported by Crouzet et al. (2010) from analysis of ASTEP South data.

Typically ASTEP 400 scientific observations start from March to the end of September for each campaign. Data acquisitions are performed automatically when the Sun elevation is lower than $-9°$. The duty cycle for the 2010-2012 campaigns of ASTEP 400 is represented in Fig. 5. The limit due to the Sun and the fraction of the science exposure observing time is shown for each day from March 12 to September 30. We acquired a total of 1959 h, 1889 h and 1997 h of science exposure frames during the 2010, 2011 and 2012 campaign respectively. This gives a duty cycle of 65.51%,
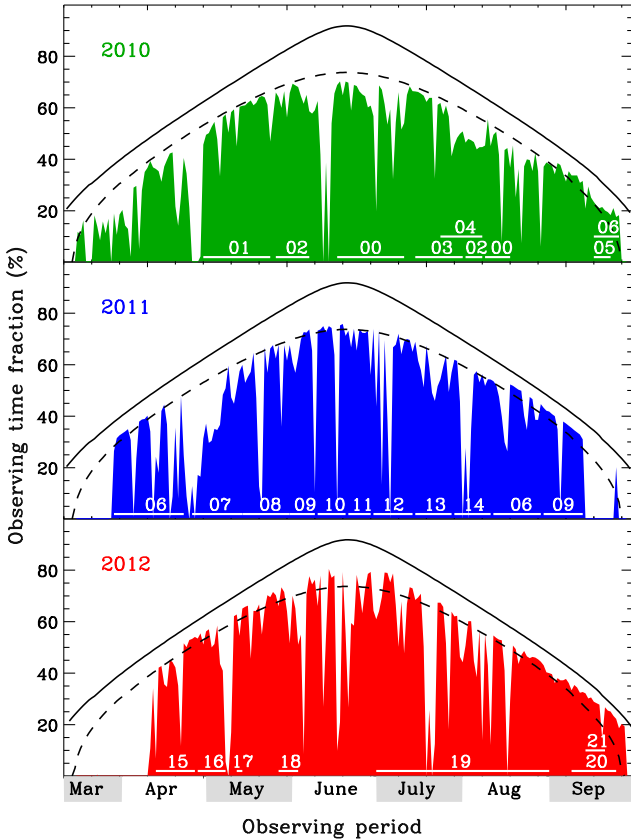
Figure 5. Daily observing time fraction for ASTEP 400 in 2010 (green), 2011 (blue) and 2012 (red) as a function of the observation period. The black solid line and dashed line indicate the fraction of time for which the Sun is lower than −9° and −13° below the horizon, respectively. Periods of observation of each field are superimposed on the corresponding plot.

Figure 6. Monthly periods of white out observed at Concordia as a function of observing period in 2010 (green), 2011 (blue) and 2012 (red). The upper plot shows the period of unavailability of ASTEP-400 due to technical issues and maintenance operations of the instrument in 2010 (green), 2011 (blue) and 2012 (red). Details of the main issues are given in Table 1. Note that the September 2011 technical issue occurred during a period of whiteout.

63.15% and 66.77% for data acquired when the Sun is lower than −9° during the 2010, 2011 and 2012 campaign respectively. When we consider only data acquired when the Sun is lower then −13°, the duty cycle reaches the values of 81.31%, 78.37% and 82.85% for 2010, 2011 and 2012 respectively. Note that we started observing late in 2012, compared to 2010 and 2011.

Figure 6 shows monthly periods during which no data has been acquired for the 2010-2012 campaigns. These phases are due either to bad weather conditions (whiteout) or to various technical issues and maintenance of the instrument. For our analysis we consider that technical and weather events are independent, even if some technical issues occur during periods of bad weather. Most maintenance operations were planned when the Sun elevation is greater than −9° and/or during poor atmospheric conditions. Periods of veiled sky and/or of poor guiding of the telescope mount, due to windy conditions, were not taken into account for this analysis, even if the observation time is even short during these periods. The main encountered technical issues were related to the power cuts lasting for a few minutes to a few hours, the mechanical adjustments of the telescope mount, particularly the first year of operation of the instrument, the failures of some electronic components, and a rare optical settings of the focal box. Figure 6 shows that the weather was better in 2010 and 2012 than in 2011. Whiteout periods of 15 days, 35 days and 19 days was observed from March 12 to September 30, on 2010, 2011 and 2012 respectively. This corresponds to a fraction of 7.4%, 17.2% and 9.3% of the total
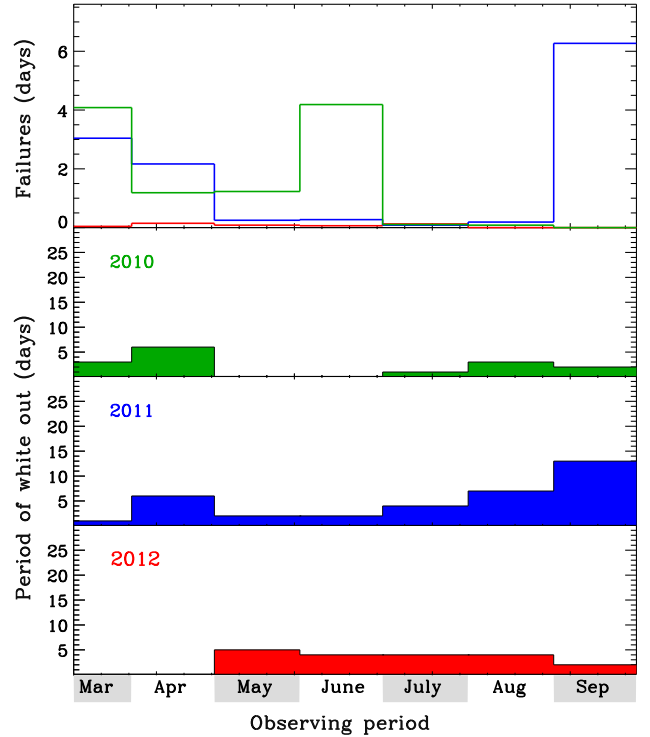
observing time. We reached a total of 10.8 days, 12.2 days and 0.45 day of various technical failures for 2010, 2011 and 2012 respectively. Table 1 gives details of typical issues that ASTEP 400 has to face with during the 2010-2012 campaigns.

Note, that the 6-day technical failures of September 2011, due to a break down of the data transfer device of the Science camera, occurred during a long period of whiteout. Figure 6 also shows that technical issues and maintenance operations decreased in 2011, excepted in September 2011, reaching a very short duration in 2012. This is the result of the continuous improvement of the instrument during its two first years of operation.

From this analysis, we found that the duty cycle for winter observations at Dome C, including bad weather and technical failures of the instrument, is greater than 60%. These results agree well with those of Crouzet et al. (2010), obtained with ASTEP South, a fixed instrument pointing towards the celestial South Pole continuously. Note that technical failures were negligible during the third year of operation of ASTEP 400. It is clear that Dome C yields a real advantage for transit search: within two weeks of observations, ASTEP 400 yields detection for planets at short periods that can only be achieved during a whole season from a temperate site (Crouzet et al. 2010; Fruth et al. 2014).

When the ASTEP program was funded by 2006, only few exoplanet transits were known and the initially expected number of transit exoplanet detection from numerical simulations was estimated to be between 10 and 15, depending of the noise level, for a 4−season ASTEP 400 operations. The ASTEP 400 initial observing strategy was tailored towards the potential of an exoplanet tran-

Table 1. Main technical issues that occured during the 2010-2012 campaigns

Tech. Issue	March (days)	April (days)	May (days)	June (days)	July (days)	August (days)	September (days)
	2010-2011-2012	2010-2011-2012	2010-2011-2012	2010-2011-2012	2010-2011-2012	2010-2011-2012	2010-2011-2012
Mecanics	0.04 - 0.00 - 0.00	0.06 - 0.00 - 0.00	0.15 - 0.00 - 0.00	0.13 - 0.02 - 0.00	0.02 - 0.00 - 0.00	0.04 - 0.00 - 0.00	0.00 - 0.00 - 0.00
Computeur	0.02 - 0.00 - 0.00	0.10 - 0.02 - 0.06	0.08 - 0.08 - 0.02	0.02 - 0.08 - 0.02	0.08 - 0.02 - 0.00	0.02 - 0.02 - 0.00	0.00 - 0.02 - 0.00
Power cuts	0.00 - 0.00 - 0.04	0.00 - 0.13 - 0.04	0.00 - 0.17 - 0.04	0.04 - 0.17 - 0.00	0.00 - 0.04 - 0.13	0.00 - 0.17 - 0.00	0.00 - 0.17 - 0.00
Electronics	0.02 - 0.04 - 0.00	0.02 - 0.02 - 0.04	0.00 - 0.02 - 0.00	0.00 - 0.00 - 0.00	0.00 - 0.02 - 0.00	0.02 - 0.00 - 0.00	0.00 - 6.08 - 0.00
Optics	4.00 - 3.00 - 0.00	1.00 - 2.00 - 0.00	1.00 - 0.00 - 0.00	4.00 - 0.00 - 0.00	0.00 - 0.00 - 0.00	0.00 - 0.00 - 0.00	0.00 - 0.00 - 0.00
Total (days)	**4.08 - 3.04 - 0.04**	**1.19 - 2.17 - 0.15**	**1.23 - 0.25 - 0.08**	**4.19 - 0.27 - 0.06**	**0.10 - 0.08 - 0.03**	**0.08 - 0.19 - 0.00**	**0.00 - 6.27 - 0.00**
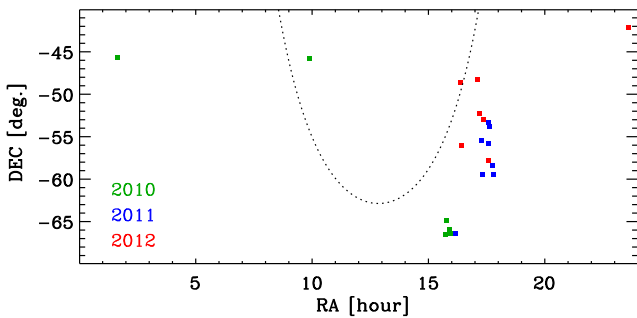
Figure 7. RA and DEC positions of fields observed during the 2010 (green), 2011 (blue) and 2012 (red) campaigns. The dotted line represents the galactic plane.

sit survey from Antarctica (Dome C) on technical, logistical and scientific aspects, observing fields, with a large number of stars, continuously. A typical field, containing ∼10 000 stars at magnitudes up to R=18, is observed during ∼7 to ∼30 days (depending on observing conditions). During the first year of ASTEP 400 operation (2010), we observed, as a test of the instrument performances, two stellar fields centered on WASP-18b and WASP-19b, two well known planetary systems. The primary goal was to retrieve the already observed transit depths, with only a few days of observation. With the on-site data processing pipeline, we realized how good the data were: i.e. the binned samples of WASP-19b lightcurve were <500 ppm (parts per million) in RMS dispersion. We then decided to increase the duration of WASP-19b observations to try to detect its secondary eclipse which depth was found to be of 390 ± 190 ppm (Abe et al. 2013). Then, we proceeded with the initial strategy observing new stellar fields searching for new exoplanetary transit candidates.

However, based on the statistically large Kepler exoplanets list, as well as on the statistics of the first years of ASTEP 400 operation, we estimated the number of new exoplanetary transits we could obtain at about 3 to 5 transits for a 4−year campaigns. Thus, the new observing strategy adapted in 2013 was to focus on fields with known exoplanet transit events, increasing the duration of observation of each field (up to 1 month), to better characterize planetary transits and to search for secondary eclipses. Figure 7 illustrates the location of the 21 stellar fields, dedicated to exoplanetary research program, we observed during the 2010-2012 winter seasons.

3   OBSERVATIONS AND DATA REDUCTION

3.1   Data processing

Each frame produced by the FLI Proline camera is 32 MiB. A typical observation "night" produces 400 to 600 frames, including calibration frames. This corresponds to more than 12 GiB of data. Each winter season produced around 6 TiB. Since the internet connection at Concordia is not sufficient for huge data transfer, all these data are transferred to France on hard disks at the end of each summer campaign. Thus, data from the winter campaign number n are available in France for processing on February of year n+1.

The Science camera produces four types of frames: science, bias, dark and "sky-flat" frames. As it is not easy to do twilight flats, nor dome flats, the photometric gain calibration is performed by using "sky-flat" frames which are obtained by taking some science frames during periods when the sky background is high i.e. when the Sun comes close to the horizon. After each of these "sky-flat" exposures, a slight random shift is applied to both the declination and right ascension axes of the telescope mount. The resulting flat frame is obtained by performing the median of all these individual exposures. By this way all stars, present on individual frames, are removed.

The ASTEP 400 data pipeline, only briefly described here (see Abe et al. (2013), for a complete description), exists under two different implementations: *i)* a custom IDL code using classical aperture photometry routines from the well known IDL astronomical library, and *ii)* Miller-Buie implementation of the Optimal Image Subtraction algorithm (OIS, Miller, Pennypacker & White (2008)). The first implementation is used for a daily on-site data processing at Concordia station, whilst the second, more computer time-consuming, is used on transferred data in France.

Each science exposure frame is bias subtracted, dark corrected, flat fielded, and the astrometric solution is computed using reference stars from the UCAC4 catalog. Aperture and OIS photometry are then performed. The OIS core algorithm is similar to the ISIS algorithm (Alard & Lupton 1998) that is known to be more accurate than aperture photometry (Montalto et al. 2007). Indeed, we found that our OIS pipeline improves the scatter in all analysed lightcurves, compared to aperture photometry, by a factor ∼1.5 in RMS, and makes the OIS data globally cleaner (Abe et al. 2013).

The OIS intrinsically removes global variations for all stars. For each field, we use a small number (typically 10) of reference stars, selected among more than 1 000 stars which not present noticeable variations, to remove systematics. The selection criteria consists in keeping those stars that minimize the most the

Table 2. The ASTEP 400 stellar fields observed during the 2010-2012 campaigns

Field	α (2000)	δ (2000)	Stars	Exp. time (s)	Date of Observation start	end	Frames	Duty cycle$^\diamond$
F-00	01:37:25.00	−45:40:40.40		15	2010-06-17	2010-07-11	44336	78%
				15	2010-08-09	2010-08-18	4484	29%
F-01	09:53:56.00	−45:46:13.50	10784	130	2010-04-30	2010-05-24	8067	79%
F-02	15:56:18.70	−66:25:24.70	13623	120	2010-05-26	2010-06-07	5891	87%
				70	2010-08-02	2010-08-08	1845	41%
F-03	15:54:48.40	−65:54:04.30	18312	70	2010-07-15	2010-08-02	7864	57%
				100	2012-08-31	2012-09-28	3622	49%
F-04	15:46:11.00	−64:53:32.59	20838	70	2010-07-24	2010-08-08	5396	50%
F-05	15:43:50.79	−66:31:13.89	18675	70	2010-09-17	2010-09-23	898	43%
F-06	16:10:51.29	−66:21:25.10	14011	70	2010-09-17	2010-09-26	3175	96%
				30	2011-03-29	2011-04-23	14490	66%
				60	2011-08-12	2011-08-18	3503	77%
				90	2011-08-19	2011-08-29	3769	81%
F-07	17:16:32.70	−55:30:04.59	16748	120	2011-04-26	2011-05-02	262	9%
				60	2011-05-03	2011-05-14	5033	56%
F-08	17:35:29.10	−55:45:47.09	12892	60	2011-05-14	2011-05-31	10957	72%
F-09	17:36:16.00	−53:48:43.09	15559	60	2011-05-31	2011-06-09	7699	82%
				120	2011-08-30	2011-09-04	1790	100%
				60	2011-09-08	2011-09-13	3146	100%
F-10	17:20:37.00	−59:26:25.79	9845	60	2011-06-10	2011-06-20	9443	87%
F-11	17:44:57.59	−58:21:16.60	9852	60	2011-06-21	2011-06-29	8495	95%
F-12	17:35:19.89	−53:21:10.39	15091	60	2011-06-30	2011-07-14	9443	67%
F-13	17:48:03.40	−59:26:52.50	8190	60	2011-07-15	2011-07-28	9781	84%
F-14	17:35:25.00	−57:51:23.10	9112	60	2011-07-29	2011-08-11	7556	74%
F-15	17:21:51.00	−53:00:22.10	17384	60	2012-04-12	2012-04-26	6928	77%
F-16	17:12:14.10	−52:17:54.90	21950	60	2012-04-27	2012-05-07	6805	88%
F-17	17:07:31.39	−48:14:53.90	23142	40	2012-05-11	2012-05-13	2210	80%
F-18	16:23:09.30	−48:38:26.20	21757	90	2012-05-26	2012-06-02	2563	44%
F-19	23:34:50.59	−42:05:27.60	613	180	2012-06-30	2012-08-31	6819	33%
F-20	16:24:16.29	−56:03:16.89	20872	90	2012-09-08	2012-09-24	2193	12%
F-21	16:28:35.09	−56:40:41.59	18431	90	2012-09-13	2012-09-20	850	40%

$^\diamond$fraction of time of science data recording including systems overheads, compared to the fraction of time when the Sun is lower than −9°.

RMS scatter after the lightcurve is normalised. We have compared this calibration procedure with other methods such as Sys-Rem (Tamuz, Mazeh & Zucker 2005), or the method described in Mazeh et al. (2009) without noticeable differences. Finally, we have applied a box-fitting algorithm (BLS: Box Least Square, Kovács, Zucker & Mazeh (2002)) to the calibrated lightcurves, to search for transits. Results presented here are from the OIS pipeline.

Observations were conducted from the beginning of March through the end of September for each season. A total of 60 stellar fields were observed during the first three years of operation of the instrument. We only focus here on the 21 stellar fields dedicated to the exoplanet transit searching program, listed in Tab. 2, for which more than 200 000 "Science" frames were processed and 310 000 stars analysed (Fig. 7).

3.2 Noise analysis

3.2.1 Noise RMS variations

In order to estimate the noise level of single nights, we computed the daily point-to-point RMS noise of ASTEP 400 data as a function of the observation period for the 2010-2012 campaigns (Fig. 8). Each point represents the median daily lightcurve RMS noise of the 10 brightest stars (R∼11 mag) of each observed field. Figure 8 shows that the daily RMS noise scatter is not uniform.

Data acquired during period around mid-season (21 June) are of poor quality. However, the median RMS noise over all nights is 1.66 mmag for the brightest stars of each field, which is close to the median RMS noise of each season. As shown in Fig. 8, there is no evident correlation between the RMS noise and the median seeing variations. Causes of RMS noise worsening could be multiple and related particularly to the consequences of mechanical and thermal changes of the structure of the instrument due to the existing harsh climatic conditions (i.e. extreme low temperatures with rapid variations), and to the large seeing variations at the ground level (Guillot et al. 2015. Submitted).

3.2.2 Correlated noise

We follow closely the approach of Pont, Zucker & Queloz (2006) in estimating the level of correlated noise present in our data. We derive the photometric precision by looking at the remaining noise in the lightcurves of stars, both point-to-point and on transit time-scale of 2.5 h, which is relevant for a hot Jupiter transiting a solar-like star. Binning, of course, will decrease the RMS of the lightcurves and help to distinguish between the two noise components: *i)* the random or white uncorrelated component, which is mainly a photon noise and *ii)* the red or correlated component, caused by systematics, mainly atmospheric conditions and telescope tracking. These parameters vary gradually over transit
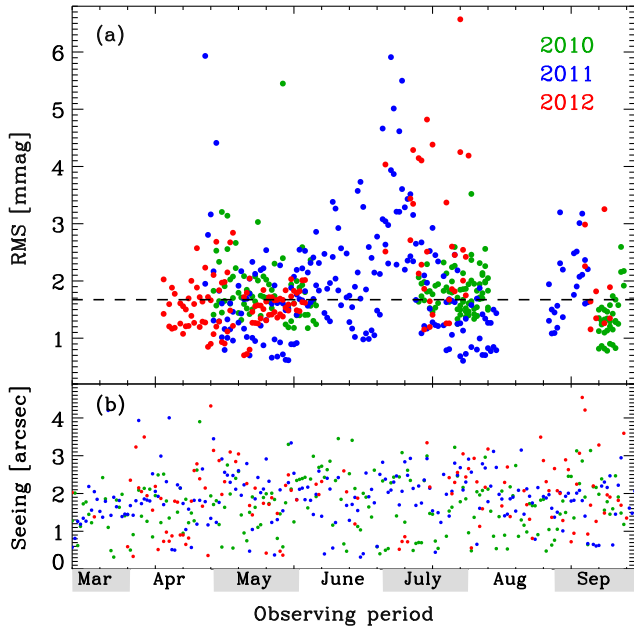
Figure 8. (a) Daily point-to-point RMS noise of ASTEP 400 data as a function of the observing period. 2010 is green, 2011 is blue and 2012 is red. The black dashed line indicates the median RMS of all data, which is close to the median RMS of each campaign. (b) Daily median seeing variations as a function of the observation period. 2010 is green, 2011 is blue and 2012 is red. Seeing, which is uniform over all season, seems not directly related to the RMS worsening observed around mid-season (21 June).

timescales and add a red noise component to the white photon noise.

We compute the running average of each lightcurve over N points (N=50) contained in a transit-length time interval of ∼2.5 h. Then we compare this curve to the RMS scatter of the individual data point divided by the square root of the average number N of observations made in this transit-length time: $\sigma_w = \sigma/\sqrt{N}$, where σ is the standard RMS noise of the whole lightcurve. For purely uncorrelated noise, these two sets of points should overlap. The amount by which the first set exceeds the second indicates the amplitude of the red noise over a transit-length timescale.

Figure 9 shows the lightcurve RMS noise vs. ASTEP 400 R-band magnitude for stars of one of the 21 stellar fields (F-01), listed in Tab. 2, together with a line tracing the theoretical photon noise limits. Lightcurves that show significant variability were removed before calculating the RMS noise. From this plot, it is clear that we have obtained a photometric precision of ∼ 2 mmag for the brightest stars (R∼12) of this field. For the dim end, the noise rises to ∼ 20 mmag at R=17 mag. Although we achieve very high photometric precision for the brightest stars, it is evident that we are well above the photon limit. Figure 9 also displays the RMS of 50-consecutive-point averages compared to the expected scatter of the same data-point averages in the presence of uncorrelated white noise. The dispersion of the mean of these 50 consecutive data points is much larger than $\sigma/\sqrt{50}$, showing that red noise dominates. The RMS scatter in the binned data is typically ∼ 500 ppm for the brightest non-variable stars, far worse than the ∼ 100 ppm that would be achieved if the noise were uncorrelated. Typically, the red noise causes the standard deviation to be ∼ 5 and ∼ 2 times larger than expected, for uncorrelated noise over transit-length timescales for bright and faint objects, respectively.

The red component of the noise in photometric data comes from the systematic errors that affect our data. These systematics, generally caused by the variations in atmospheric conditions, the telescope tracking and the detector characteristics, introduce some covariance between the lightcurve data points, with time-scales similar to the duration of planetary transits. At Dome C, a large part of systematic errors are caused by the seeing variations at the ground level and by the rapid temperature fluctuations. ASTEP 400, which is located at ∼2 m above the ground level, is very sensitive to these fluctuations in winter.

Pont, Zucker & Queloz (2006) introduced a parameter called σ_r, to characterize the amplitude of the red noise for each lightcurve and discussed methods of characterizing the structure of the covariance matrix for a given stellar lightcurve. The covariance structure of the correlated noise is quantified by the power-law dependence of the RMS scatter on the number N of data points used in the box smoothing:

$$\sigma_N = \sigma N^b$$

where σ_N is the RMS scatter of the smooth lightcurve and σ the RMS scatter of the N individual data points. For totally uncorrelated noise, b=−0.5, while for fully correlated noise the RMS scatter should be independent of the number of data points, giving b=0. We plot, in Fig. 9, b as a function of ASTEP 400 R-band magnitude. As expected, effects of correlated noise are most pronounced for the brightest stars of the observed field. Even at our faint cut-off limit of R∼18 Mag. However, we do not recover the uncorrelated noise value of b=−0.5.

Fruth et al. (2014) compared joint observations of the well-known exoplanet WASP-18b and two target fields from Antarctica (ASTEP 400) and Chile (BEST II) with a particular attention paid to the photometric precision and to the phase observational coverage. The photometric systems of the two instruments are expected to be similar, both instruments using the same CCD chip and both observing in wide spectral band. Fruth et al. (2014) showed that for bright targets (e.g. WASP-18b) ASTEP 400 data show a smaller noise level compared to BEST II. However, the difference is not on the order of a factor of 2-4, as expected from a smaller scintillation noise, indicating that systematic effects contribute significantly to the noise budget of ASTEP 400. Moreover, an analysis of two large data sets of both telescopes showed that their photometric precision is very similar, with a slight advantage for ASTEP 400.

Surface-based turbulent layers with a depth, lower than 5 m, between 5 m and 20 m, and higher than 20 m, are observed at Dome C, for 17%, 38% and 45% of time, respectively (Petenko et al. 2014), confirming previous result of (Aristidi et al. 2009). ASTEP 400, which is installed at about 2 m above the snow surface, is almost embedded inside this turbulent boundary layer. Our photometric data are therefore affected by the rapid temperature fluctuations and by the quite poorness of the seeing at that level. Installing the telescope above the turbulent surface layer could reduce systematic effects, but solutions should be found to avoid these atmospheric disturbances. To understand how temperature gradients and seeing fluctuations affect our results, we conducted some calculations of thermal deformations of the telescope and analysed their expected consequences for turbulence on the optical path of the instrument (Guillot et al., 2015. Submitted). We also conducted some specific tests during the summer campaign to identify how some subsystems could affect the image quality of the telescope and thus the photometric data quality. We found that dilatations of the telescope, due to the large temperature variations,
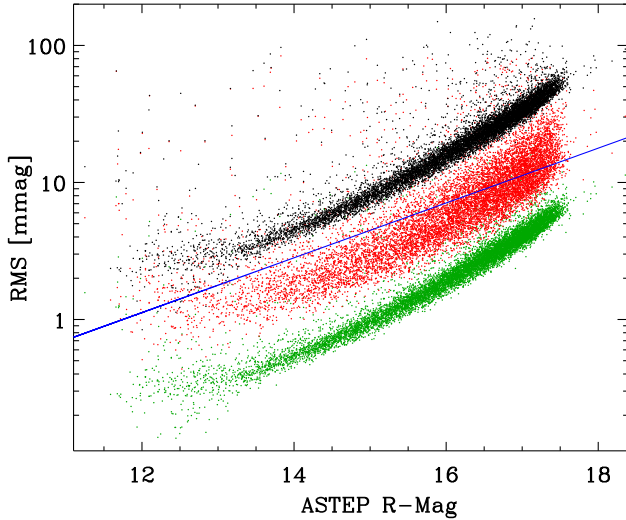
Figure 9. Typical photometric precision attained with ASTEP 400, as established from the point-to-point RMS of the lightcurves after 3σ rejection of outlier points. Each point represents a lightcurve. Objects are those of one of the first stellar fields (F-01) containing more than 10 000 stars observed during the 2010 season. The upper group of symbols (black) shows the point to point RMS of lightcurves for each star, the middle group (red) shows the RMS in the same lightcurves after performing a moving weighted average over transit-length time intervals (2.5 h) and the lower group (green) shows the expected RMS for uncorrelated noise (RMS scatter of the individual data point divided by the square root of the average number N of points (N=50) in a 2.5-h intervals). The correlated noise amplitude among the brightest stars is $\sim$2 mmag. The dotted (blue) line shows the theoretical limits (photon noise).

and the heating of the mirrors, necessary to prevent frost, are the main causes of the PSF extra-broadening, even if a special care is taken to limit the temperature gradient heating of the mirrors. From this analysis, we identified some ways to improve the ASTEP 400 instrument. These improvements (i.e. mirrors ventilated with dry air, focal plane adjusted in real time, tip-tilt system and/or telescope installed at a higher level...) should equip any future telescope operating in Antarctica (Guillot et al., 2015. Submitted).

4 TRANSIT SEARCHING AND FOLLOW-UP OBSERVATIONS

4.1 Transit searching

To search for possible planetary transits, we performed a box least-square (BLS) period search (Kovács, Zucker & Mazeh 2002) on lightcurves of each stellar field. BLS allows fast and efficient searching for transits and provides rank ordered lists of the best lightcurves based on SNR. We then visually inspected all the selected lightcurves to eliminate those that show unusual variations or other systematic problems. We have selected systems that present transit-like features in their folded lightcurves, and excluded those with transit depths indicating very large planetary radius or showing secondary-eclipse features. We have also rejected stars with close (<3") brighter companion. From this analysis, we found 43 transit candidates and more than 1 900 variables stars which will be presented in a forthcoming paper (Mékarnia et al. in preparation). Tab. 3 lists the ASTEP 400 and UCAC4 identifications, coordinates, V, R magnitudes (from UCAC4), J, H, K magnitudes (from
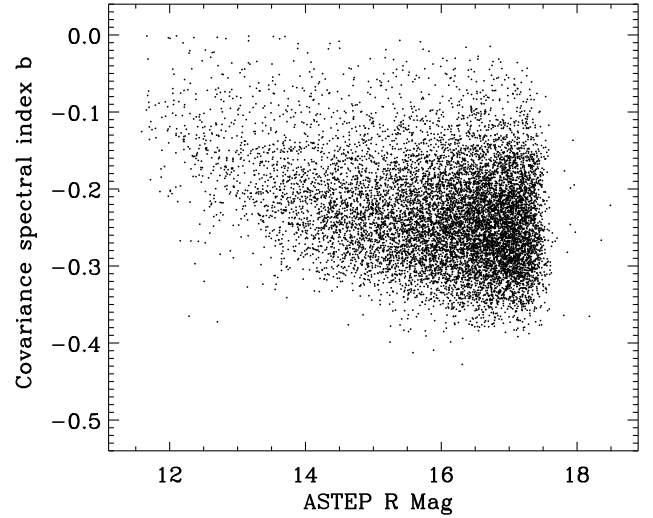

Figure 10. Covariance spectral index b as a function of ASTEP 400 R-band magnitude. Pure uncorrelated (white) noise should give b=−0.5, while pure correlated noise should give b=0. We see that effects of correlated noise are more pronounced for the brightest stars of our field.

2MASS) and corresponding observed field for each exoplanet transit candidate.

For each candidate system, a transit model was fit to the data. We used the analytic formulae of Mandel & Agol (2002) to model the transit and a Keplerian orbit to model the orbital phase. The model fits for the orbital period, the epoch of the detected event, the depth and length of the transit, the inclination of the orbit as well as the scaled planetary radius ($r_p/R_\star$). In addition, we used the independently stellar densities ρ_t and ρ_{JK} calculated from transit parameters and J-K colors, respectively, to identify the most promising transiting exoplanet candidates, as described in Tingley, Bonomo & Deeg (2011). Results are listed in Tab. 4.

4.2 Follow-up observations

Radial velocity (RV) follow-up is needed to identify the nature of the transiting object and establish the mass of the planet and the eccentricity of its orbit. This can be done by measuring the RV variation, which is directly linked to the mass ratio of the main star to its companion. We performed spectroscopic observations for 19 of the 43 exoplanetary transit candidates using the Wide Field Spectrograph (WiFeS; Dopita et al. (2007, 2010)) on the Australian National University (ANU) 2.3 m telescope at Siding Spring Observatory. One planet transit candidate (C-1) was observed using the spectrograph HARPS, which is mounted full time on the 3.6 m telescope in La Silla, ESO, Chile (Rupprecht et al. (2004)).

For candidates observed with WIFES, our strategy was to first take a low resolution (R=3 000) flux calibrated spectrum for spectral typing, to vet for false-positive scenarios involving giants. We then take multi-epoch R=7 000 radial velocity measurements, timed at phase quadrature, to check for velocity variations at the km s^{-1} level that would point to the candidate being an EcB. The full reduction procedure is detailed in Penev et al. (2013). Since WiFeS is an integral field spectrograph with 38"x11" FoV, spectra for nearby companions to the candidates are also extracted and analyzed in the same way. There are instances where we find con-

Table 3. List of selected ASTEP 400 exoplanet transit candidates

Cand.	ASTEP ID	UCAC4 ID	α (J2000)	δ (J2000)	V (mag)	R (mag)	J (mag)	H (mag)	K (mag)	Field
C-1	A-031-1432-1080	U4-117-120529	16:12:28.315	−66:36:02.63	12.25	12.17	11.16	10.93	10.86	F-06
C-2	A-009-0788-3195	U4-223-043932	09:55:20.070	−45:25:11.28	14.13	14.48	13.11	12.84	12.73	F-01
C-3	A-009-3827-0876	U4-220-040923	09:50:53.391	−46:00:56.61	16.50	16.21	15.54	15.12	15.10	F-01
C-4	A-009-2480-1645	U4-221-041868	09:52:51.825	−45:49:12.82	16.20	15.19	14.84	14.19	14.11	F-01
C-5	A-020-0766-3182	U4-122-142653	15:57:59.214	−65:36:10.80	15.13	14.92	13.46	12.79	12.63	F-03
C-6	A-020-3351-3239	U4-123-150641	15:51:34.427	−65:35:29.20	13.91	-	13.40	13.00	12.86	F-03
C-7	A-012-2686-3723	U4-121-140615	15:54:39.519	−65:59:38.21	14.55	15.56	14.30	14.01	13.87	F-02/F-03
C-8	A-012-2616-1638	U4-118-126574	15:54:48.844	−66:31:44.37	13.63	14.03	13.54	13.32	13.23	F-02
C-9	A-042-1493-1784	U4-181-196452	17:37:14.849	−53:52:32.05	17.01	13.59	11.97	11.54	11.40	F-09
C-10	A-040-3806-1347	U4-171-187216	17:32:16.625	−55:56:28.52	15.88	15.88	14.20	13.66	13.52	F-08
C-11	A-042-1344-1819	U4-181-196513	17:37:30.457	−53:51:57.76	12.50	12.54	11.35	11.14	11.08	F-09
C-12	A-009-3640-2734	U4-223-042828	09:51:10.060	−45:32:26.09	14.43	14.08	12.58	11.95	11.79	F-01
C-13	A-009-2138-2068	U4-222-041279	09:53:22.093	−45:42:39.95	16.06	16.01	15.23	15.01	14.85	F-01
C-14	A-037-2105-3878	U4-175-188215	17:16:24.977	−55:01:43.88	14.57	14.88	13.53	13.10	13.06	F-07
C-15	A-045-2152-2821	U4-185-192986	17:35:08.888	−53:09:03.26	13.03	13.06	12.05	11.76	11.72	F-12
C-16	A-012-3270-0293	U4-116-118563	15:53:06.940	−66:52:15.10	13.81	14.54	13.53	13.17	13.10	F-02
C-17	A-037-3129-2829	U4-174-179953	17:14:34.749	−55:17:53.50	13.54	-	12.88	12.55	12.45	F-07
C-18	A-045-3805-0481	U4-182-189991	17:32:18.784	−53:44:58.85	15.77	15.48	14.58	14.22	14.10	F-12
C-19	A-021-2548-0316	U4-124-144094	15:44:59.381	−65:19:55.89	15.22	13.32	13.37	12.87	12.80	F-04
C-20	A-021-2298-0771	U4-124-144273	15:45:35.965	−65:12:59.85	13.22	12.96	12.53	12.28	12.28	F-04
C-21	A-021-1387-1097	U4-125-146829	15:47:49.670	−65:07:55.19	14.39	14.24	13.64	13.38	13.27	F-04
C-22	A-042-0935-3675	U4-184-191506	17:38:09.963	−53:23:21.14	14.55	14.62	13.32	12.78	12.78	F-09/F-12
C-23	A-042-3059-3753	U4-184-190549	17:34:31.233	−53:22:21.21	15.57	14.98	14.43	14.08	14.01	F-09/F-12
C-24	A-053-2846-0663	U4-187-172292	17:10:56.154	−52:39:24.58	13.37	13.60	12.44	12.03	11.94	F-16
C-25	A-053-2656-1277	U4-188-174569	17:11:15.161	−52:29:59.66	14.00	-	13.14	12.57	12.29	F-16
C-26	A-053-1172-1642	U4-188-175770	17:13:45.373	−52:24:14.90	13.29	13.33	12.68	12.41	12.35	F-16
C-27	A-054-3685-2190	U4-209-133083	17:05:02.534	−48:12:51.69	12.99	13.07	11.71	11.48	11.42	F-17
C-28	A-055-3107-3596	U4-209-116230	16:21:32.534	−48:14:51.00	14.01	13.93	12.47	12.05	11.92	F-18
C-29	A-055-2846-1800	U4-207-115393	16:21:56.195	−48:42:28.08	15.09	14.11	13.33	12.86	12.69	F-18
C-30	A-055-2093-0212	U4-205-119263	16:23:07.250	−49:06:49.57	15.73	14.62	12.23	11.46	11.24	F-18
C-31	A-055-1859-0987	U4-206-118241	16:23:28.945	−48:54:58.28	13.73	12.89	12.36	11.87	11.77	F-18
C-32	A-055-0363-0217	U4-205-120592	16:25:48.735	−49:06:21.85	14.49	14.39	14.03	13.64	13.58	F-18
C-33	A-055-3499-1964	U4-207-114982	16:20:55.462	−48:39:55.04	13.19	12.36	9.47	8.60	8.31	F-18
C-34	A-055-2130-3575	U4-209-116840	16:23:02.739	−48:15:05.86	14.58	14.22	12.62	12.20	12.08	F-18
C-35	A-055-1859-1579	U4-207-116242	16:23:28.773	−48:45:51.11	14.47	14.14	13.65	13.31	13.17	F-18
C-36	A-055-3989-2702	U4-208-120345	16:20:10.887	−48:28:32.88	15.93	15.24	12.23	11.31	10.83	F-18
C-37	A-055-1449-2398	U4-208-122291	16:24:06.661	−48:33:08.74	14.90	14.60	13.60	13.38	13.22	F-18
C-38	A-055-1334-1279	U4-206-118679	16:24:18.054	−48:50:25.44	-	14.48	13.06	12.72	12.53	F-18
C-39	A-055-1429-3231	U4-209-117316	16:24:07.807	−48:20:19.14	15.39	13.94	12.26	11.52	11.32	F-18
C-40	A-055-3438-0492	U4-205-118143	16:21:01.325	−49:02:28.89	14.44	13.94	12.29	11.83	11.68	F-18
C-41	A-055-0903-3693	U4-209-117629	16:24:55.664	−48:13:14.91	14.89	14.46	13.43	13.07	12.87	F-18
C-42	A-055-3244-1770	U4-207-115121	16:21:19.075	−48:42:54.86	14.91	14.36	12.32	11.60	11.40	F-18
C-43	A-055-3403-3609	U4-209-116070	16:21:05.445	−48:14:40.70	15.12	15.00	13.08	12.56	12.39	F-18

Note. Units of right ascension are hours, minutes, and seconds, and units of declination are degrees, arcminutes, and arcseconds.

tamination from a nearby eclipsing binary (EcB) to be the cause of the photometric signal.

We match each observed flux calibrated spectrum against a grid of synthetic spectra from the Munari library, fitting for T_{eff}, log g and [Fe/H]. For each grid point, the RMS of fit is calculated. We preferentially weight log g sensitive regions (e.g. Balmer jump for hotter stars, Mgb and MgH regions for cooler stars) during the grid fitting, so that we can confidently differentiate between dwarfs and giants. We also account for interstellar extinction by iterating the fit over the possible reddening values up to the Schlegel maximum for the region.

On the basis of these observations, it is possible to conclude that: *i)* the following transit candidates: C-2, C-11, C-14, C-15, and C-21, which are dwarfs showing no RV variations within $2\,\mathrm{km\,s^{-1}}$,

are a possible good planetary candidates pending future detailed investigations, and the transit candidates, C-3 and C-22, which are dwarfs that show no RV variations within $5\,\mathrm{km\,s^{-1}}$, need more accurate RV observations to confirm their possible planetary status; *ii)* the following transit candidates: C-1, C-5, C-6, C-7, C-8, C-12, C-16, C-17 and C-20 are rejected as eclipsing binaries. On the other hand, incomplete follow-up observations do not allow to obtain any information on the planetary status of C-4, C-10, C-19, and C-23. In addition, following the ρ_t/ρ_{JK} vs. transit depth relation as described by Tingley, Bonomo & Deeg (2011), and as RV observations have not yet been conducted, we can select the following systems: C-9, C-13, C-24, C-27, C-35 and C-37 as possible good planetary candidates that need future RV observations.
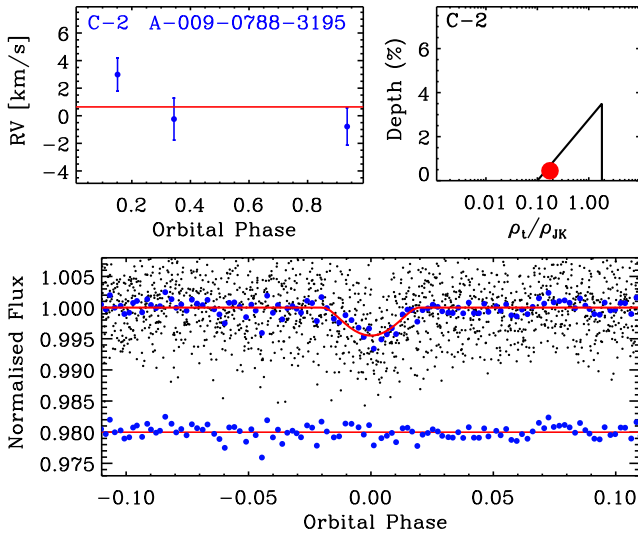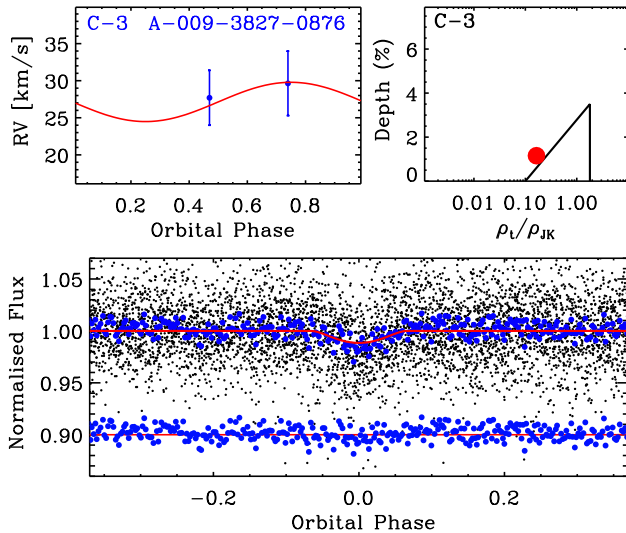
Figure 11. Phase-folded lightcurve, RV measurements and $\rho_t/\rho_\star$ vs. transit depth relation of the possible good planet candidate C-2. The lower figure represents the transits of C-2 compared to the best-fit model using transit parameters listed in Tab. 4 (residuals of the fit are plotted at the bottom of the figure, offset from zero). Upper figures show RV measurements for C-2 from ANU as a function of orbital phase, together with our best fit model indicating no significant RV variation within $2\,\mathrm{km\,s^{-1}}$ level, the zero phase corresponding to the time of mid-transit. The $\rho_t/\rho_\star$ vs. transit depth relation shows that C-2 is a good planetary candidate.

Figure 12. Phase-folded lightcurve, RV measurements and $\rho_t/\rho_\star$ vs. transit depth relation of the possible good planet candidate C-3. The lower figure represents the transits of C-3 compared to the best-fit model using transit parameters listed in Tab. 4 (residuals of the fit are plotted at the bottom of the figure, offset from zero). Upper figures show RV measurements for C-3 from ANU as a function of orbital phase, together with our best fit model indicating no significant RV variation within $5\,\mathrm{km\,s^{-1}}$ level, the zero phase corresponding to the time of mid-transit. We need a point at phase 0.25 to confirm this result. The $\rho_t/\rho_\star$ vs. transit depth relation shows that C-3 is a good planetary candidate.
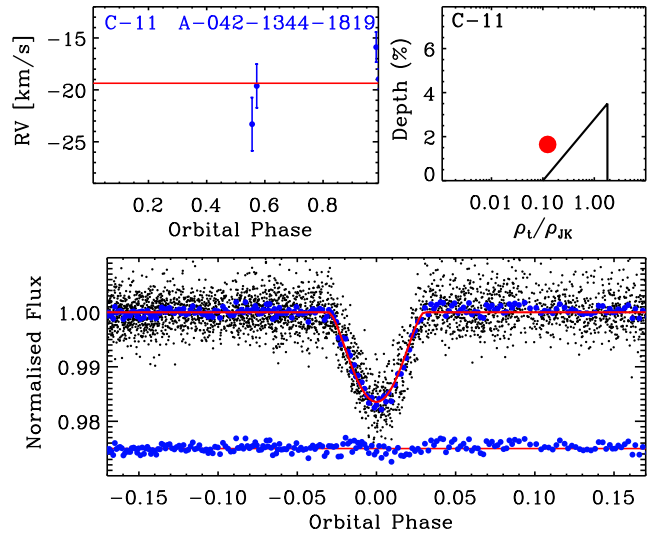

Figure 13. Phase-folded lightcurve, RV measurements and $\rho_t/\rho_\star$ vs. transit depth relation of the possible good planet candidate C-11. The lower figure represents the transits of C-11 compared to the best-fit model using transit parameters listed in Tab. 4 (residuals of the fit are plotted at the bottom of the figure, offset from zero). Upper figures show RV measurements for C-11 from ANU as a function of orbital phase, together with our best fit model indicating no significant RV variation within $2\,\mathrm{km\,s^{-1}}$ level, the zero phase corresponding to the time of mid-transit. The $\rho_t/\rho_\star$ vs. transit depth relation shows that C-11 should be a good planetary candidate.

5 PROPERTIES OF CANDIDATES

Here we present the ASTEP 400 transit candidates along with a brief overview over the properties of the star and the detected transit signal. Any follow-up observations that have been performed are also described. Tab. 4 summarizes the transit parameters of all candidates, while Tab. 5 only gives properties of the parent stars of followed-up candidates. The candidates are presented in the following order: we focus first on the possible good planetary candidates that show no RV variations within $2\,\mathrm{km\,s^{-1}}$ and $5\,\mathrm{km\,s^{-1}}$ levels (Fig. 11 to 17). Then, we present candidates with large RV variations non-compatible with exoplanets (Fig. 18 to 20) and systems with spectroscopic and/or RV observations not accurate enough or incomplete to determine their planetary status. Finally, we present candidates not yet followed-up (Fig. 21 to 26). Figures 29 and 30 show images centered on each exoplanet transit candidate, extracted from the ASTEP 400 reference frame of the corresponding observed field.

5.1 Followed-up possible good planetary candidates

C-2 (A-009-0788-3195, UCAC4 223-043932) is located in the field F-01. It is a relatively bright star (V=14.1 mag) with a 0.45% deep transit occurring every 2.43 d for duration of 2.4 h. A total of 6 transits were detected for this system. There is no bright source (up to V=16 mag) close to this candidate and blending can be ruled out (Fig. 29). From spectroscopic measurements, we found the star is a dwarf with a T_{eff}=6134±100 K and no RV variation at $2\,\mathrm{km\,s^{-1}}$ level. The ratio of stellar density calculated from transit parameters to this from J-K colors is ρ_t/ρ_{JK}=0.1 agreeing well with the $\rho_t/\rho_\star$ vs. transit depth relation for known exoplanets as described by Tingley, Bonomo & Deeg (2011) (Fig. 11).
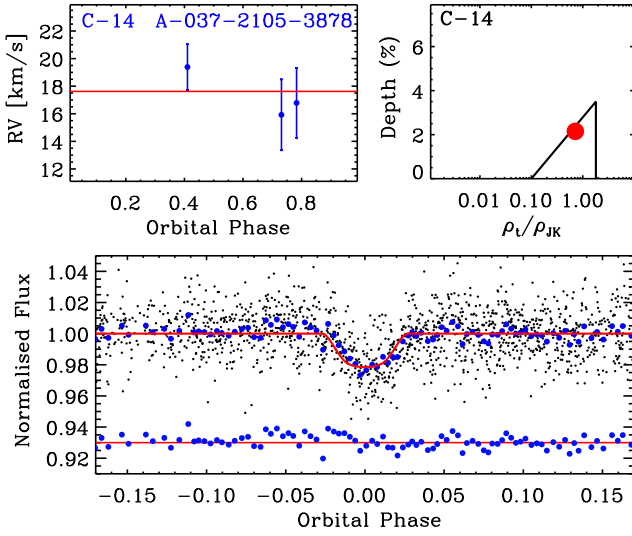
Figure 14. Phase-folded lightcurve, RV measurements and $\rho_t/\rho_\star$ vs. transit depth relation of the possible good planet candidate C-14. The lower figure represents the transits of C-14 compared to the best-fit model using transit parameters listed in Tab. 4 (residuals of the fit are plotted at the bottom of the figure, offset from zero). Upper figures show RV measurements for C-14 from ANU as a function of orbital phase, together with our best-fit model indicating no significant RV variation within 2km s^{-1} level, the zero phase corresponding to the time of mid-transit. The $\rho_t/\rho_\star$ vs. transit depth relation shows that C-14 is a good planetary candidate.

C-3 (A-009-3827-0876, UCAC4 220-040923), which is located in the field F-01, is relatively faint (V=16.5 mag) and has no close companion (up to V=17 mag) (Fig. 29). We detected 24 transit events with a depth of 1.31% and a period of 0.53 d, for this candidate (Fig. 12). This star is a dwarf (T$_{eff}$=6683±100 K, log g=4.0±0.5) and presents no RV variation at 5 km s^{-1} level. The ratio of stellar density calculated from transit parameters to this from J-K colors is ρ_t/ρ_{JK}=0.15 close to the $\rho_t/\rho_\star$ vs. transit depth relation for known exoplanets as described by Tingley, Bonomo & Deeg (2011).

C-11 (A-042-1344-1819, UCAC4 181-196513) is located in the field F-09. This bright object (V=12.5 mag) has a depth of 1.6% and a period of 2.16 d for transit duration of 3 h. The star, which shows no significant RV variation at 2 km s^{-1} level, has an ambiguous gravity with a log g=2.6±0.5, of probably a subgiant. A total of 5 V-shape transit events were detected for this system. The $\rho_t/\rho_\star$ vs. transit depth relation of this candidate is close to that of known exoplanets as described by Tingley, Bonomo & Deeg (2011) (Fig. 13). There is no bright source (up to V=17) close to this target (Fig. 29).

C-14 (A-037-2105-3878, UCAC4 175-188215) is located in the field F-07. We detected 5 transit events of this relatively bright star (V=14.6 mag). The ASTEP 400 lightcurve shows a 2.14% deep transit occurring every 1.47 d. ANU spectroscopy classifies this candidate as dwarf, with no RV variation at 2 km s^{-1} level. In addition, the $\rho_t/\rho_\star$ vs. transit depth relation of this target agrees very well with that of an exoplanet system (Fig. 14). There is no bright source close to this candidate (Fig. 29).

C-15 (A-045-2152-2821, UCAC4 185-192986). We detect 5 transit events of this relatively bright (V=13.0 mag) candidate
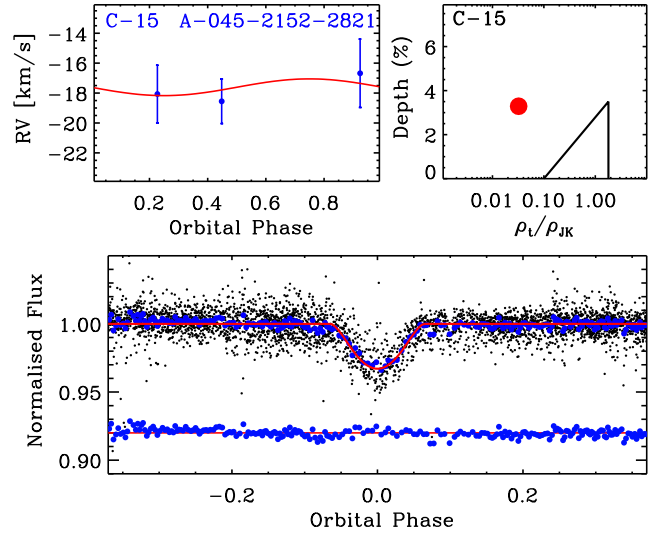

Figure 15. Phase-folded lightcurve, RV measurements and $\rho_t/\rho_\star$ vs. transit depth relation of the possible good planet candidate C-15. The lower figure represents the transits of C-15 compared to the best-fit model using transit parameters listed in Tab. 4 (residuals of the fit are plotted at the bottom of the figure, offset from zero). Upper figures show RV measurements for C-15 from ANU as a function of orbital phase, together with our best-fit model indicating no significant RV variation within 2km s^{-1} level, the zero phase corresponding to the time of mid-transit.
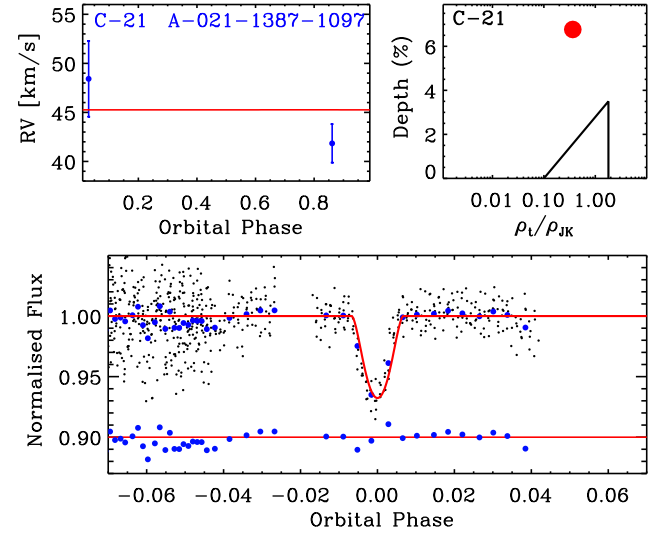

Figure 16. Phase-folded lightcurve, RV measurements and $\rho_t/\rho_\star$ vs. transit depth relation of the possible good planet candidate C-21. The lower figure represents the transits of C-21 compared to the best-fit model using transit parameters listed in Tab. 4 (residuals of the fit are plotted at the bottom of the figure, offset from zero). Upper figures show RV measurements for C-21 from ANU as a function of orbital phase, together with our best fit model indicating no significant RV variation within 2km s^{-1} level, the zero phase corresponding to the time of mid-transit.

located in the field F-12. C-15 has a 2.9% deep transit signal, a period of 1.37 d and a transit duration of 4 h. Frp spectroscopic measurements, we classify this star as dwarf, with log g=4.0±0.5 and T$_{eff}$=6193±100 K. We found no significant RV variation at 2 km s^{-1} level, even if the $\rho_t/\rho_\star$ vs. transit depth relation of this candidate does not agree with that of an exoplanet (Fig. 15). There
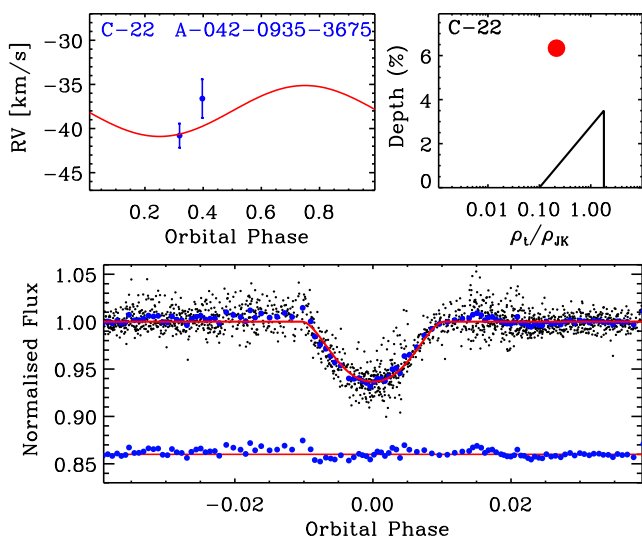
Figure 17. Phase-folded lightcurve, RV measurements and $\rho_t/\rho_\star$ vs. transit depth relation of the possible good planet candidate C-22. The lower figure represents the transits of C-22 compared to the best-fit model using transit parameters listed in Tab. 4 (residuals of the fit are plotted at the bottom of the figure, offset from zero). Upper figures show RV measurements for C-22 from ANU as a function of orbital phase, together with our best fit model indicating no significant RV variation within $5\,\mathrm{km\,s^{-1}}$ level, the zero phase corresponding to the time of mid-transit.

is a close-by faint companion (V=18) 2" away (Fig. 29).

C-21 (A-021-1387-1097, UCAC4 125-146829). We detect two transit events of this bright (V=14.4 mag) candidate located in the field F-04. C-21 has 5.8% deep transit signal, a period of 11.77 d and transit duration of 4.15 h. The star, which presents no RV variation within $2\,\mathrm{km\,s^{-1}}$ level, is found as giant with a T_{eff}=5560±100 K and a log g=4.0±0.5, from spectroscopic measurements. The $\rho_t/\rho_\star$ vs. transit depth relation of this target suggest an eclipsing binary scenario (Fig. 16). There is a faint giant star that has no significant RV variation at $2\,\mathrm{km\,s^{-1}}$ level, close to this target (Fig. 29).

C-22 (A-042-0935-3675, UCAC4 184-191506) is a relatively bright candidate (V=14.5 mag) located in both fields F-09 and F-13. We detected 2 transit events with a period of 3.10 d, a depth of 6.42% and duration of 5.14 h (Fig. 17). C-22 is a dwarf (T_{eff}=5823±100 K, log g=4.0±0.5, [Fe/H]=−0.5±0.5) and has $\rho_t/\rho_\star$ vs. transit depth relation that does not agree with that of exoplanet.

5.2 Followed-up non-planetary candidates

C-1 (A-031-1432-1080, UCAC4 117-120529) is located in the field F-06. It is a bright star (V=12.2 mag) with a 1.32% deep transit occurring every 2.05 d for duration of 2.17 h (Fig. 18). A total of 3 transits were detected for this system. From HARPS measurements we obtained a radial velocity of $35\,\mathrm{km\,s^{-1}}$. We concluded that C-1 is very likely an eclipsing binary.

C-5 (A-020-0766-3182, UCAC4 122-142653) is located in the field F-03. It is a relatively bright (V=15.1 mag) star, with no close bright companion (Fig. 29). We detected 14 transit events with a

depth of 1.37%, a period of 0.67 d and duration of 1.60 h (Fig. 18). C-5 is rejected as giant.

C-6 (A-020-3351-3239, UCAC4 123-150641) is located in the field F-03. It is a relatively bright (V=13.9 mag) star, with a close faint companion. We detected 4 transit events with a depth of 2.44% a period of 4.99 d and a duration of 2.67 h (Fig. 18). From spectroscopic measurements, we found this candidate is a dwarf with a radial velocity of $30\,\mathrm{km\,s^{-1}}$ and a high eccentricity orbit. C-6 is rejected as eclipsing binary. The close-by companion is a dwarf, but no usable radial velocity was derived. A third fainter neighbor is present, but no usable spectrum was extracted.

C-7 (A-012-2686-3723, UCAC4 121-140615) is a candidate with a close-by companion (V=13.6 mag) located both in the field F-02 and F-03. We detected 3 transit events with a depth of 6.01%, a period of 3.34 d and duration of 2.36 h (Fig. 19). We found that C-7 is a dwarf, with a T_{eff}=5272±100 K, log g=4.4±0.5, [Fe/H]=−0.5±0.5 and a radial velocity of $4\,\mathrm{km\,s^{-1}}$. The close-by companion has a radial velocity of $30\,\mathrm{km\,s^{-1}}$ and an orbit in phase with the transit period. C-7 was rejected as blended eclipsing binary.

C-8 (A-012-2616-1638, UCAC4 118-126574) is a relatively bright (V=13.6 mag) candidate located in the field F-02, with faint close companion (Fig. 29). We detected 9 transit events with a depth of 1.97%, a period of 1.76 d and duration of 2.47 h (Fig. 19). C-8 is a dwarf or a subgiant with a radial velocity of $26\,\mathrm{km\,s^{-1}}$ and an orbit in phase with the transit period. C-8 is rejected as an eclipsing binary.

C-12 (A-009-3640-2734, UCAC4 223-042828) is located in the field F-01. This relatively bright candidate (V=14.4 mag) has a very close companion (<2", V-Mag ∼16) (Fig. 29). We detected 8 transit events for this candidate. The C-12 lightcurve shows a 0.45% deep transit occurring every 1.63 d and transit duration of 3.75 h (Fig. 19). C-12 (T_{eff}=4283±100 K, log g=2.3±0.5, [Fe/H]=0.0±0.5) was rejected as giant.

C-16 (A-012-3270-0293, UCAC4 116-118563) is located in the field F-02. It is a relatively bright (V=13.8 mag) star with no close companion (Fig. 29). C-16 is a dwarf. It was rejected as eclipsing binary, following its radial velocity of $21\,\mathrm{km\,s^{-1}}$ and an orbit in phase with the transit events (Fig. 20).

C-17 (A-037-3129-2829, UCAC4 174-179953). We detect two transit events of this relatively bright (V=13.5 mag) candidate located in the field F-07. We found a period of 12.43 d, a transit depth of 4.6% and duration of 8.7 h (Fig. 20). C-17 is probably a subgiant (T_{eff}=6009 K) which presents an ambiguous gravity (log g=3.1±0.5). This candidate has a radial velocity of $36\,\mathrm{km\,s^{-1}}$ and was rejected as an eclipsing binary. No spectral type was derived from its close companion that shows no radial velocity variation within $2\,\mathrm{km\,s^{-1}}$.

C-20 (A-021-2298-0771, UCAC4 124-144273). We detect 2 transit events of this relatively bright (V=13.2 mag) candidate, located in the field F-04, which has a very close (< 2") faint (V∼17) and a close (< 3") bright (V=13.4 mag) companions (Fig. 20 and Fig. 29). C-20 is a dwarf with a T_{eff}=6925±100 K, log g=4.9±0.5 and [Fe/H]=0.0±0.5. We found a radial velocity of ∼15 km s^{-1}, but more data are needed to confirm this result. The close-by

Table 4. Transit parameters of ASTEP 400 exoplanet candidates

Cand.	Period (d)	Duration (hr)	Depth (mag)	Epoch (2 455 000.0+)	Ntr	Inclination (deg.)	$R_\star$ ($R_\odot$)	R_P ($R_\odot$)	ρ_t (g cm^{-3})	ρ_{JK} (g cm^{-3})	ρ_t/ρ_{JK}	Comment
C-1	2.052300	2.35176	0.01308	458.139828	3	75.96	2.25	0.40	0.20	0.80	0.25	b
C-2	2.431040	2.08932	0.00449	318.223836	6	75.96	2.67	0.29	0.14	0.96	0.15	a
C-3	0.527440	1.54458	0.01156	318.240229	24	56.31	2.52	0.43	0.16	1.04	0.15	a
C-4	0.621550	1.97846	0.01415	318.360373	24	57.99	2.97	0.45	0.11	1.71	0.07	c
C-5	0.671310	1.66674	0.01373	392.298537	14	64.76	2.08	0.31	0.23	3.34	0.07	b
C-6	4.996360	2.67186	0.02442	393.908462	4	84.29	1.39	0.33	0.52	1.14	0.46	b
C-7	3.343030	2.89441	0.04605	397.929364	3	82.79	1.43	0.41	0.49	1.03	0.48	b
C-8	1.763220	2.46950	0.01971	342.883252	9	87.63	1.05	0.14	0.90	0.82	1.10	b
C-9	0.865980	0.85058	0.00366	713.243979	16	74.05	1.16	0.12	0.74	1.17	0.64	d
C-10	1.247150	1.60236	0.03707	696.885791	7	82.79	0.85	0.16	1.39	1.44	0.97	c
C-11	2.165480	3.07228	0.01646	714.385468	5	74.05	2.90	0.58	0.12	0.74	0.16	a
C-12	1.636140	3.74976	0.00449	318.358074	8	56.31	7.81	0.86	0.02	2.13	0.01	b
C-13	3.979750	2.61466	0.02948	319.920625	5	88.40	0.79	0.13	1.60	0.96	1.67	d
C-14	1.476060	1.80420	0.02150	680.422692	5	80.95	1.16	0.17	0.75	1.07	0.70	a
C-15	1.372470	4.06290	0.03291	743.870682	3	64.76	4.26	1.02	0.06	0.86	0.06	a
C-16	6.592460	5.03627	0.05174	346.429294	2	90.00	1.39	0.29	0.52	1.03	0.50	b
C-17	12.436400	8.88110	0.04511	692.255946	2	87.76	2.80	0.56	0.13	1.03	0.12	b
C-18	1.004750	3.16624	0.03190	743.022285	6	67.42	3.12	0.59	0.10	1.08	0.10	d
C-19	0.448820	1.77151	0.03076	402.139402	22	59.68	2.14	0.43	0.22	1.17	0.19	c
C-20	11.377900	9.10598	0.05378	406.128735	2	87.28	2.93	0.65	0.12	0.70	0.17	b
C-21	11.768100	3.72996	0.06766	406.023841	2	87.93	0.91	0.27	1.22	0.94	1.30	a
C-22	14.777800	6.91931	0.06338	715.969968	2	87.05	2.12	0.57	0.22	1.14	0.19	a
C-23	5.523710	4.55295	0.07338	717.123045	2	85.49	1.65	0.46	0.37	1.02	0.36	c
C-24	0.503500	0.99367	0.00654	1045.205249	10	76.17	0.85	0.07	1.38	1.10	1.26	d
C-25	0.666610	1.78238	0.01918	1045.404875	11	64.76	2.07	0.37	0.23	4.10	0.06	d
C-26	1.491980	4.55916	0.02890	1046.085967	4	67.42	4.63	0.83	0.05	0.86	0.05	d
C-27	1.347080	2.64624	0.01096	1059.210623	2	80.43	1.80	0.18	0.31	0.78	0.39	d
C-28	0.418390	1.67804	0.00757	1061.294808	37	45.00	3.67	0.51	0.07	1.15	0.06	d
C-29	1.098130	2.93618	0.00644	1062.107732	13	56.31	5.24	0.68	0.04	1.32	0.03	d
C-30	1.206200	4.30019	0.02443	1061.234866	14	56.31	5.76	1.38	0.03	27.60	0.00	d
C-31	1.299940	2.60684	0.00554	1061.475853	12	64.76	4.03	0.36	0.06	1.19	0.05	d
C-32	1.417800	2.79806	0.01638	1061.839131	13	75.25	2.39	0.31	0.17	1.05	0.17	d
C-33	1.565540	2.98996	0.00451	1061.744802	10	64.76	4.85	0.39	0.04	68.40	0.00	d
C-34	1.662470	3.96885	0.01211	1062.394636	8	64.76	5.16	0.72	0.04	1.14	0.03	d
C-35	2.091910	2.27422	0.00900	1061.717085	9	85.19	1.11	0.10	0.82	1.08	0.76	d
C-36	2.146180	5.32857	0.01373	1062.283283	7	64.76	6.66	1.00	0.02	126.00	0.00	d
C-37	2.342440	2.32634	0.01646	1062.750690	6	78.69	1.84	0.37	0.30	0.96	0.31	d
C-38	2.753900	3.92076	0.02523	1063.258084	6	84.85	1.87	0.28	0.29	1.13	0.25	d
C-39	3.236520	8.65382	0.00879	1061.733064	4	56.31	15.45	2.32	0.00	15.60	0.00	d
C-40	3.299310	4.88344	0.01394	1062.302144	4	78.77	3.62	0.43	0.08	1.23	0.06	d
C-41	3.587360	5.48108	0.02067	1064.730933	4	74.85	4.81	0.91	0.04	1.16	0.04	d
C-42	5.265950	4.86099	0.02472	1064.620779	2	81.01	3.14	0.66	0.10	10.80	0.01	d
C-43	6.972090	3.38945	0.02444	1066.916567	3	84.81	1.68	0.40	0.36	1.47	0.24	d

(a): Possible good planetary candidate. *(b)*: Rejected as eclipsing binary. *(c)*: Spectral and/or RV observations do not allow to obtain the planetary status of the candidate. *(d)*: No RV observations.

bright companion is a dwarf (T_{eff}=6228±100 K, log g=4.4±0.5, [Fe/H]=−0.5±0.5) and shows no radial variation within 2 km s^{-1}.

5.3 Other followed-up candidates

C-4 (A-009-2480-1645, UCAC4 221-041868) is a faint object (V=16.2 mag) located in the field F-01. We detected 24 transit events for this candidate with a depth of 1.4% and a period of 0.62 d (Fig. 21). From spectroscopic measurements, we found the star is probably a subgiant with an ambiguous gravity (log g=3.0±0.5). The ratio of stellar density calculated from transit parameters to this from J-K color is ρ_t/ρ_{JK}=0.07 and does not agree with the $\rho_t/\rho_\star$ vs. transit depth relation for known exoplanets as described

by Tingley, Bonomo & Deeg (2011).

C-10 (A-040-3806-1347, UCAC4 171-187216) is located in the field F-08. This candidate which is relatively faint (V=15.9 mag) has a close (6") companion with the same brightness (Fig. 29). We detected 7 transit events with a depth of 3.57%, a period of 1.25 d and transit duration of 1.42 h (Fig. 21). This candidate (T_{eff}=5295±100 K, [Fe/H]=−0.5±0.5), which presents an ambiguous gravity (log g=3.5±0.5), is probably a subgiant. The close-by companion is a dwarf (T_{eff}=4566±100 K, log g=4.1±0.5, [Fe/H]=−0.5±0.5).

C-19 (A-021-2548-0316, UCAC4 124-144094) is a faint candidate (V=15.2 mag) located in the field F-04. We detected 22 V-shape
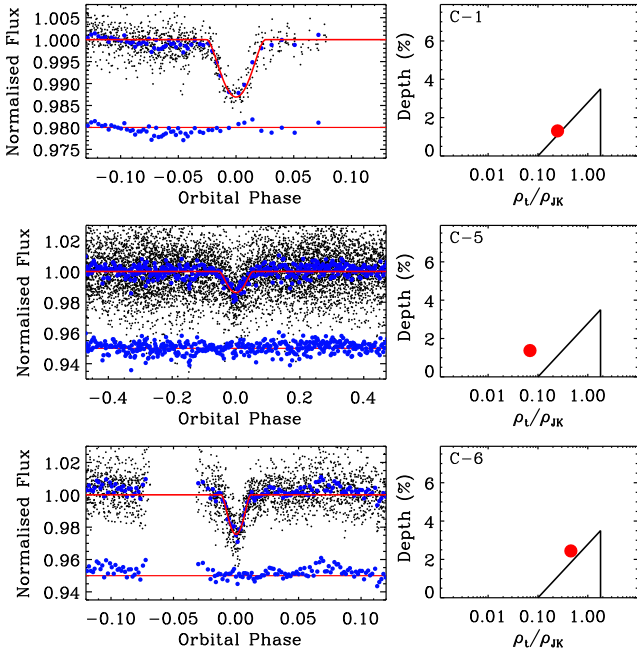
Figure 18. Phase-folded light-curves of the candidates C-1, C-5, and C-6, rejected as non planetry systems from RV measurements, compared to the best-fit model using transit parameters listed in Tab. 4. Residuals of the fit are plotted at the bottom of the figure, offset from zero.
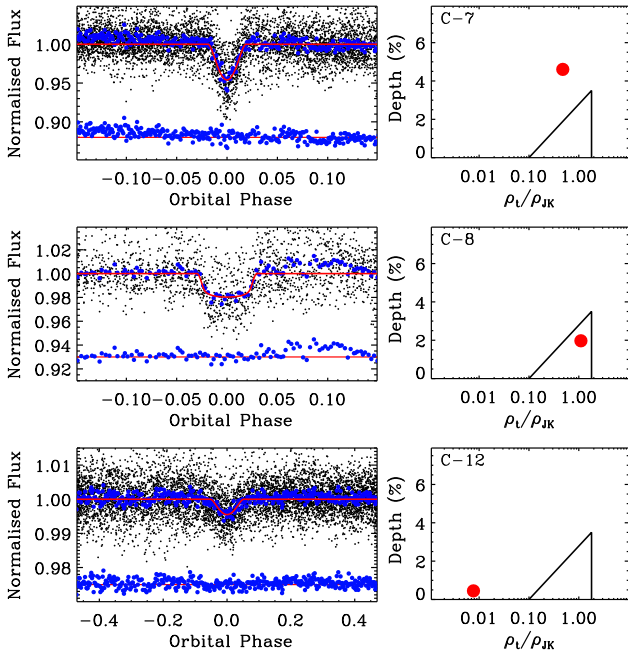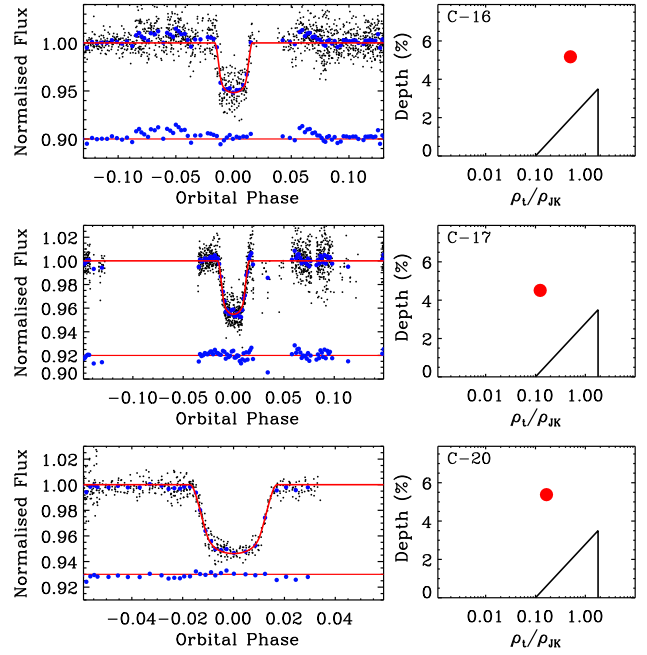

Figure 19. Phase-folded light-curves of the candidates C-7, C-8 and C-12, rejected as non planetary systems from RV measurements, compared to the best fit model using transit parameters listed in Tab. 4. Residuals of the fit are plotted at the bottom of the figure, offset from zero.

Figure 20. Phase-folded lightcurves and the $\rho_t/\rho_\star$ vs. transit depth relation of the candidates C-16, C-17 and C-20, rejected as non-planetary systems from RV measurements, compared to the best-fit model using transit parameters listed in Tab. 4. Residuals of the fit are plotted at the bottom of the figure, offset from zero.

transit events with a period of 0.45 d, a depth of 3.36% and duration of 1.77 h. No radial velocity measurements were performed for this target which has $\rho_t/\rho_\star$ vs. transit depth relation that not agree with that of exoplanet (Fig. 21). However future investigations are needed to characterize the nature of this candidate.

C-23 (A-042-3059-3753, UCAC4 184-190549), which is located in the field F-09, has a faint (V~17 mag) very close (<2") companion (Fig. 30). C-23 is a dwarf (T_{eff}=6281±100 K, log g=3.9±0.5, [Fe/H]=−0.5±0.5). Its companion also is a dwarf (T_{eff}=5735±100 K, log g=3.5±0.5, [Fe/H]=0.0±0.5). We detected 2 transit events for this target with a period of 5.52 d and a transit depth of 7.33%. The $\rho_t/\rho_\star$ vs. transit depth relation of C-23 suggest an eclipsing binary scenario (Fig. 21).

5.4 Candidates not yet followed-up

5.4.1 Possible good planetary candidates

C-9 (A-042-1493-1784, UCAC4 181-196452) We detect 16 transit events of this faint (V=17.0 mag) star located in the field F-09. C-9 has a 0.34% deep transit signal with a period of 0.86 d and transit duration of 0.78 h. The $\rho_t/\rho_\star$ vs. transit depth relation of this target strongly suggest an exoplanet scenario (Fig. 22). No RV observations were performed for this target, and future investigations are needed to confirm its planetary nature. There is no bright close companion to this candidate.

C-13 (A-009-2138-2068, UCAC4 222-041279). This relatively faint (V=16.1 mag) candidate, located in the field F-01, has 2.9% deep transit signal, a period of 3.98 d and a transit duration of 2.61 h. 5 transit events were detected for this candidate, but its

Table 5. Stellar parameters of spectroscopic follow-up candidates

ASTEP Cand.	ASTEP ID	T_{eff} [*] (K)	log g[*]	[Fe/H][*]	K (km s^{-1})	Comments
C-1	A-031-1432-1080				35	Rejected as EcB (V=35 km s^{-1}, M=0.22 M⊙).
C-2	A-009-0788-3195	6134	4.4	0.0		Dwarf. No RV variation within 2km s^{-1}.
C-3	A-009-3827-0876	6683	4.0	-0.5		Dwarf. No RV variation within 5km s^{-1}. Needs a point at 0.25 phase to confirm.
C-4	A-009-2480-1645	5033	3.0	-0.5		Ambiguous gravity (subgiant?). Large RV variation not in phase with the ephemeris.
C-5	A-020-0766-3182	4245	1.8	-0.5		Rejected as Giant.
C-6	A-020-3351-3239	6692	4.3	-0.5	30	Dwarf. Rejected as EcB.
C-7	A-012-2686-3723	5272	4.4	-0.5	4	Dwarf. Rejected as EcB.
C-8	A-012-2616-1638	6066	3.4	-0.5	26	Dwarf (subgiant?). Rejected as EcB.
C-10	A-040-3806-1347	5295	3.5	-0.5		Ambiguous gravity (subgiants?).
C-11	A-042-1344-1819	6249	2.6	-0.5		Dwarf (subgiant?). No RV variation within 2 km s^{-1}.
C-12	A-009-3640-2734	4283	2.3	0.0		Rejected as Giant.
C-14	A-037-2105-3878	5941	4.0	0.0		Dwarf. No RV variation within 2 km s^{-1}
C-15	A-045-2152-2821	6193	4.0	-0.5		Dwarf. No RV variation within 2 km s^{-1}. Close-by faint companion 2" away.
C-16	A-012-3270-0293	6230	4.4	-0.5	21	Dwarf. Orbit in phase, rejected as EcB.
C-17	A-037-3129-2829	6009	3.1	0.0	36	Ambiguous gravity (subgiant?). Rejected as EcB
C-19	A-021-2548-0316					No usable spectral typing exposure obtained. No RV variation within 5 km s^{-1}.
C-20	A-021-2298-0771	6925	4.9	0.0	20	Dwarf. Rejected as EcB.
C-21	A-021-1387-1097	5560	4.0	-0.5		Dwarf. No RV variation within 2 km s^{-1}.
C-22	A-042-0935-3675	5823	4.0	-0.5		Dwarf. No RV variation within 5 km s^{-1}.
C-23	A-042-3059-3753	6281	3.9	-0.5		Dwarf. No RV measurements obtained.

[*] Error is 100 K for T_{eff}, 0.5 for log g and 0.5 for [Fe/H].

phase folded lightcurves remains incomplete due to its orbital period which is close to a multiple of 1 d. However, the $\rho_t/\rho_\star$ vs. transit depth relation of this target is compatible with an exoplanet scenario (Fig. 22). No RV observations were conducted on this candidate.

C-24 (A-053-2846-0663, UCAC4 187-172292) is a bright candidate (V=13.4 mag) located in the field F-16. It has a faint close (<10") companion (Fig. 30). We detected 10 transit events for this target with a period of 0.503 d and a transit depth of 0.66%. No radial velocity observations were performed for this candidate which has $\rho_t/\rho_\star$ vs. transit depth relation that agree very well with that of a exoplanet (Fig. 22).

C-27 (A-054-3685-2190, UCAC4 209-133083) is a bright candidate (V=13.0 mag) located in the field F-17. It has a faint (V∼16) close (∼ 5") companion (Fig. 29). We detected 2 transit events for this target with a period of 1.347 d and a transit depth of 0.95% (Fig. 23). No radial velocity observations were performed for this candidate which has $\rho_t/\rho_\star$ vs. transit depth relation that agree well with that of an exoplanet.

C-35 (A-055-1859-1579, UCAC4 207-116242) is a relatively bright candidate (V=14.5 mag) located in the field F-18. There are some faint close (< 3") stars to this target (Fig. 30). We detected 9 transit events for this target with a period of 2.09 d and a transit depth of 0.93% (Fig. 23). No radial velocity observations were performed for this candidate which presents a $\rho_t/\rho_\star$ vs. transit depth relation that agree well with that of an exoplanet.

C-37 (A-055-1449-2398, UCAC4 208-122291) is a candidate (V=14.9 mag) located in the field F-18 with no close (< 8") companions (Fig. 30). We detected 6 transit events for this target with a period of 2.34 d and a transit depth of 1.64%. No radial velocity observations were performed for this candidate which presents a $\rho_t/\rho_\star$ vs. transit depth relation that does not agree with

that of an exoplanet (Fig. 23).

5.4.2 Other planetary candidates

C-18 (A-045-3805-0481, UCAC4 182-189991) is a faint candidate (V=15.8 mag) located in the field F-12. We detected 6 V-shape transit events with a period of 1.005 d, a depth of 3.19% and duration of 3.16 h. No radial velocity measurements were performed for this candidate which has $\rho_t/\rho_\star$ vs. transit depth relation that not agree with that of a exoplanet (Fig. 24). However future investigations are needed to characterize the nature of this candidate.

C-25 (A-053-2656-1277, UCAC4 188-174569) is located in the field F-16. It has a faint (V∼16 mag) very close (< 2") companion (Fig. 30). We detected 11 V-shape transit events for this target with a period of 0.666 d and a transit depth of 1.91% (Fig. 24). No radial velocity observations were performed for this target which has $\rho_t/\rho_\star$ vs. transit depth relation that does not agree with that of an exoplanet.

C-26 (A-053-1172-1642, UCAC4 188-175770) is a bright candidate (V=13.2 mag) located in the field F-16. It has a bright (V∼13) companion located at (∼6") (Fig. 30). We detected 4 V-shape transit events for this target with a period of 1.492 d and a transit depth of 2.89% (Fig. 24). No radial velocity observations were performed for this target which has $\rho_t/\rho_\star$ vs. transit depth relation that does not agree with that of an exoplanet.

C-28 (A-055-3107-3596, U4-209-116230) is a bright candidate (V=14.0 mag) located in the field F-18. We detected 37 transit events for this target with a period of 0.418 d and a transit depth of 0.75%. No radial velocity observations were performed for this candidate which presents a $\rho_t/\rho_\star$ vs. transit depth relation that does
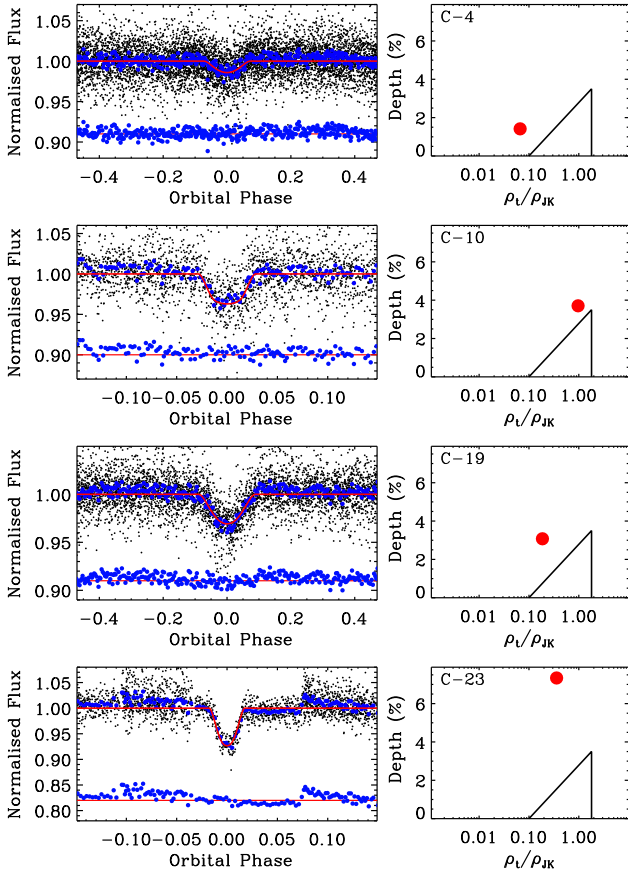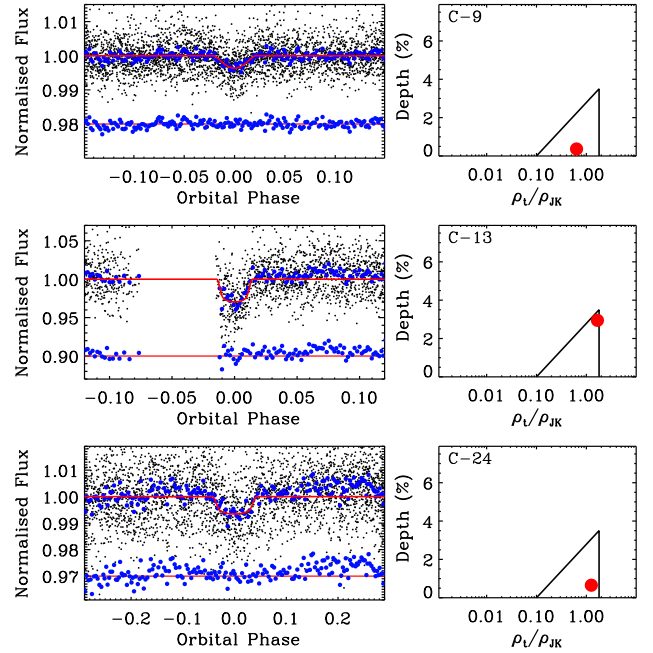
Figure 21. Phase-folded lightcurves of the transits of candidates C-4, C-10, C-19, and C-23, for which spectral and/or RV observations do not allow to obtain information on their planetary status, compared to the best-fit model using transit parameters listed in Tab. 4. Residuals of the fit are plotted at the bottom of the figure, offset from zero.

not agree well with that of an exoplanet (Fig. 25).

C-29 (A-055-2846-1800, UCAC4 207-115393) is a candidate (V=15.0 mag) located in the field F-18. It has a faint (V∼17 mag) close (<3") to this target (Fig. 30). We detected 13 V-shaped transit events for this target with a period of 1.098 d and a transit depth of 0.69%. No radial velocity observations were performed for this candidate which presents a $\rho_t/\rho_\star$ vs. transit depth relation that does not agree well with that of an exoplanet (Fig. 25).

C-30 (A-055-2093-0212, UCAC4 205-119263) is a candidate (V=15.7) located in the field F-18. There is a faint (V∼17 mag) close (<6") to this target (Fig. 30). We detected 14 V-shaped transit events for this target with a period of 1.206 d and a transit depth of 2.44% (Fig. 25). No radial velocity observations were performed for this candidate which presents a $\rho_t/\rho_\star$ vs. transit depth relation that does not agree well with that of an exoplanet.

C-31 (A-055-1859-0987, UCAC4 206-118241) is a candidate (V=13.7 mag) located in the field F-18. There is a relatively bright (V∼14) star very close (<2") to this target. We detected 12 V-shaped transit events for this target with a period of 1.299 d and a transit depth of 0.55% (Fig. 26). No radial velocity observations were performed for this target which presents a $\rho_t/\rho_\star$ vs. transit

Figure 22. Phase-folded lightcurves of the transits of candidates C-9, C-13, and C-24, which could be possible good planetary candidates following the $\rho_t/\rho_\star$ vs. transit depth relation as described by by Tingley, Bonomo & Deeg (2011), compared to the best-fit model using transit parameters listed in Tab. 4. Residuals of the fit are plotted at the bottom of the figure, offset from zero.
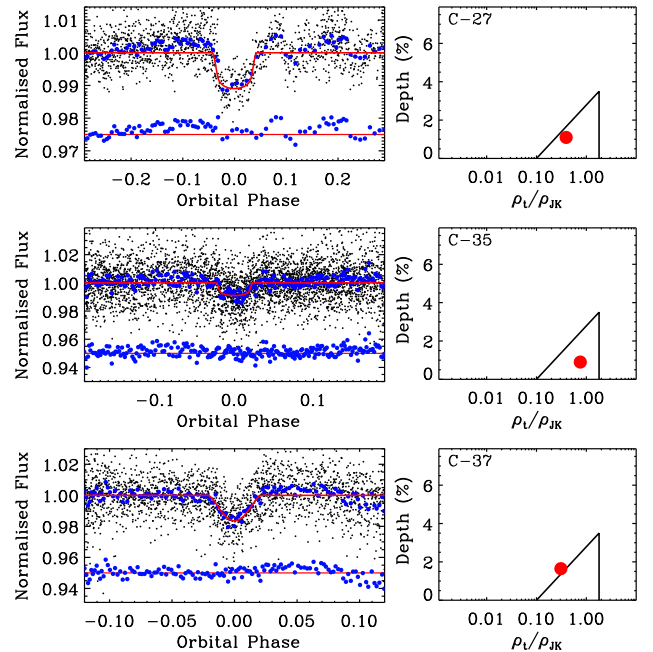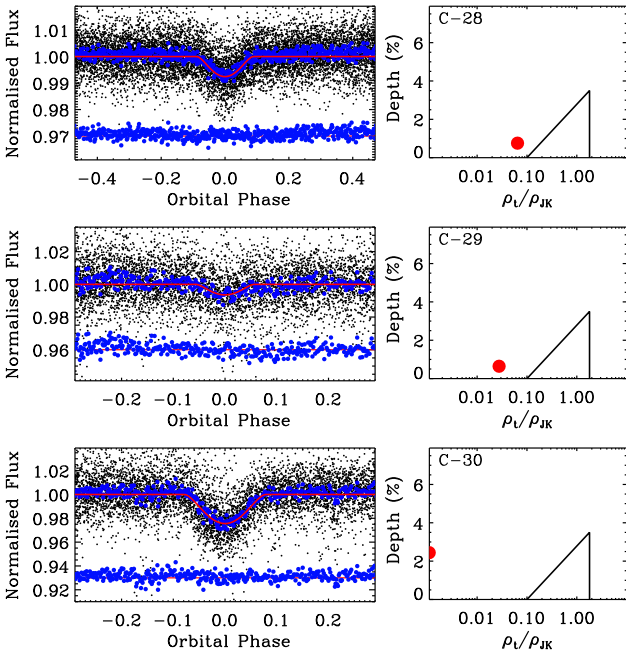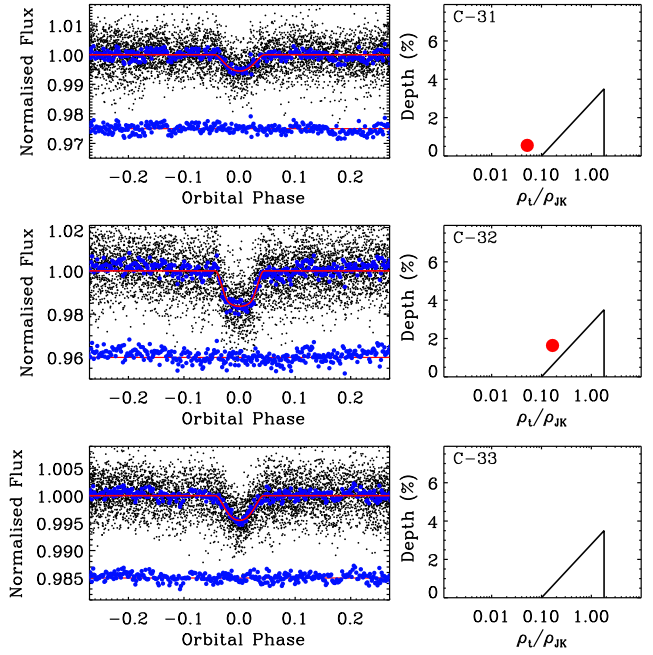

Figure 23. Phase-folded lightcurves of the transits of candidates C-27, C-35, and C-37, which could be possible good planetary candidates following the $\rho_t/\rho_\star$ vs. transit depth relation as described by by Tingley, Bonomo & Deeg (2011), compared to the best-fit model using transit parameters listed in Tab. 4. Residuals of the fit are plotted at the bottom of the figure, offset from zero.
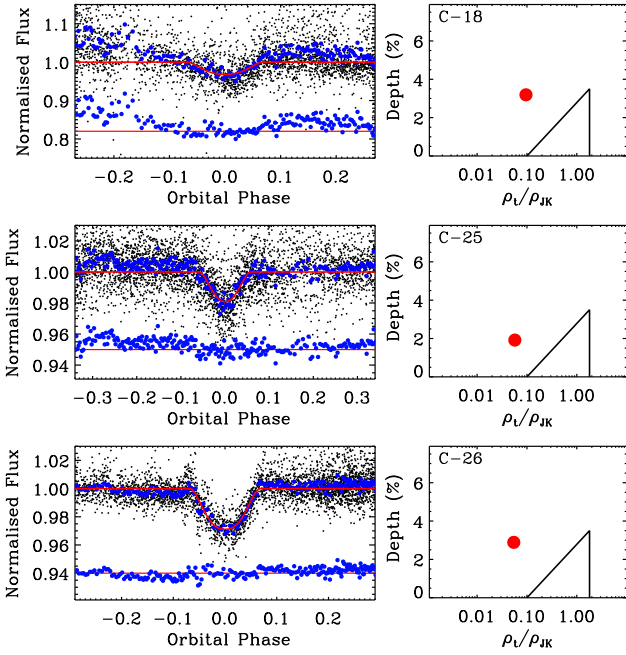
Figure 24. Phase-folded lightcurves of the transits of candidates C-18, C-25, and C-26, non yet followed-up, compared to the best-fit model using transit parameters listed in Tab. 4. Residuals of the fit are plotted at the bottom of the figure, offset from zero.

Figure 26. Phased light-curve of the transits of candidates C-31, C-32 and C-33, non yet followed-up, compared to the best-fit model using transit parameters listed in Table 4. Residuals of the fit are plotted at the bottom of the figure, offset from zero.

Figure 25. Phase-folded lightcurves of the transits of candidates C-28, C-29, and C-30, non yet followed-up, compared to the best-fit model using transit parameters listed in Tab. 4. Residuals of the fit are plotted at the bottom of the figure, offset from zero.

depth relation that does not agree well with that of an exoplanet.

C-32 (A-055-0363-0217, UCAC4 205-120592) is a bright candidate (V=14.5 mag) located in the field F-18. There are some faint (V~18-19) stars close (< 3") to this target. We detected 13 transit events for this target with a period of 1.417 d and a transit depth of 1.64% (Fig. 26). No radial velocity measurements were performed for this candidate which presents a $\rho_t/\rho_\star$ vs. transit depth relation that does not agree well with that of an exoplanet.

C-33 (A-055-3499-1964, UCAC4 207-114982) is a bright candidate (V=13.2 mag) located in the field F-18 with no evident close (< 10") star. We detected 10 transit events for this target with a period of 1.565 d and a transit depth of 0.45% (Fig. 26). No radial velocity observations were performed for this candidate which presents a $\rho_t/\rho_\star$ vs. transit depth relation that does not agree well with that of an exoplanet.

C-34 (A-055-2130-3575, UCAC4 209-116840) is a relatively bright candidate (V=14.5 mag) located in the field F-18 with no close (< 10") star. We detected 8 transit events for this target with a period of 1.66 d and a transit depth of 1.21% (Fig. 27). No radial velocity observations were performed for this candidate which presents a $\rho_t/\rho_\star$ vs. transit depth relation that does not agree well with that of an exoplanet.

C-36 (A-055-3989-2702, UCAC4 208-120345) is a faint candidate (V=15.9 mag) located in the field F-18 with no close (< 10") stars. We detected 7 transit events for this target with a period of 2.15 d and a transit depth of 1.37%. No radial velocity observations were performed for this candidate which presents a $\rho_t/\rho_\star$ vs. transit depth relation that does not agree with that of an exoplanet
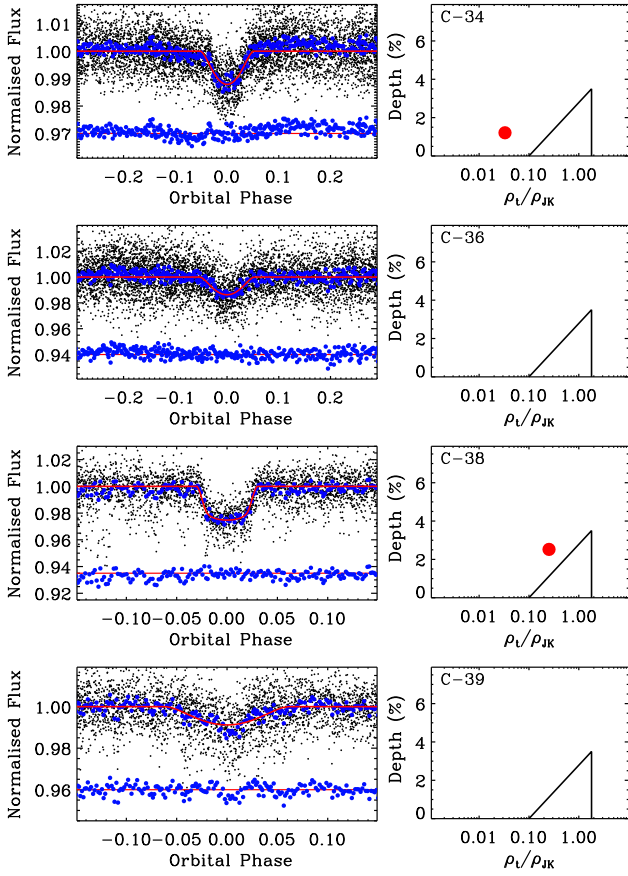
Figure 27. Phased lightcurves of the transits of candidates C-34, C-36, C-38, and C-39, non yet followed-up, compared to the best-fit model using transit parameters listed in Table 4. Residuals of the fit are plotted at the bottom of the figure, offset from zero.
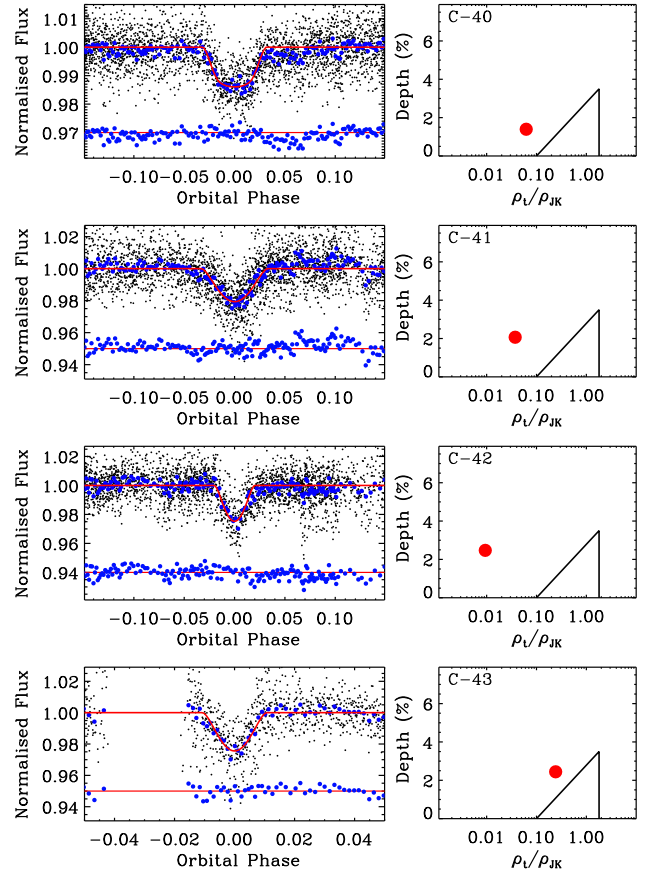
Figure 28. Phase-folded lightcurves of the transits of candidates C-40, C-41, C-42, and C-43, non yet followed-up, compared to the best-fit using transit parameters listed in Table 4. Residuals of the fit are plotted at the bottom of the figure, offset from zero.

(Fig. 27).

C-38 (A-055-1334-1279, UCAC4 206-118679) is a candidate (V=14.5 mag) located in the field F-18 with no close (< 10") stars. We detected 6 transit events for this target with a period of 2.75 d and a transit depth of 2.52%. No radial velocity observations were performed for this candidate which presents a $\rho_t/\rho_\star$ vs. transit depth relation that does not agree with that of an exoplanet (Fig. 27).

C-39 (A-055-1429-3231, UCAC4 209-117316) is a faint candidate (V=15.4 mag) located in the field F-18. There is a faint star close (< 3") to this target. We detected 4 transit events for this target with a period of 3.23 d and a transit depth of 0.88%. No radial velocity observations were performed for this candidate which presents a $\rho_t/\rho_\star$ vs. transit depth relation that does not agree with that of an exoplanet (Fig. 27).

C-40 (A-055-3438-0492, UCAC4 205-118143) is a relatively bright candidate (V=14.4 mag) located in the field F-18. There is a faint star close (< 3") to this target. We detected 4 transit events for this target with a period of 3.30 d and a transit depth of 1.39%. No radial velocity measurements were performed for this candidate which presents a $\rho_t/\rho_\star$ vs. transit depth relation that does not agree with that of an exoplanet (Fig. 28).

C-41 (A-055-0903-3693, UCAC4 209-117629) is a candidate (V=14.9 mag) located in the field F-18 with no evident close (< 10") companion. We detected 4 transit events for this target with a period of 3.58 d and a transit depth of 2.06%. No radial velocity measurements were performed for this candidate which presents a $\rho_t/\rho_\star$ vs. transit depth relation that does not agree with that of an exoplanet (Fig. 28).

C-42 (A-055-3244-1770, UCAC4 207-115121) is a candidate (V=14.9 mag) located in the field F-18. There is a faint star close (< 3") to this target. We detected 2 transit events for this target with a period of 5.26 d and a transit depth of 2.22%. No radial velocity observations were performed for this candidate which presents a $\rho_t/\rho_\star$ vs. transit depth relation that does not agree with that of an exoplanet (Fig. 28).

C-43 (A-055-3403-3609, UCAC4 209-116070) is a candidate (V=15.1 mag) located in the field F-18 with no evident close (< 5") companion. We detected 3 transit events for this target with a period of 6.97 d and a transit depth of 2.44%. No radial velocity observations were performed for this candidate which presents a $\rho_t/\rho_\star$ vs. transit depth relation that does not agree with that of an exoplanet (Fig. 28).

6   SUMMARY AND CONCLUSIONS

ASTEP 400 is a 40 cm telescope, dedicated to finding and characterizing transiting exoplanets. It is designed to withstand the harsh climatic conditions at Dome C, achieving an extremely stable photometric accuracy of a fraction of milli-magnitude and providing near-continuous observations for the entire duration of the Antarctic winter night. ASTEP 400 is semi-robotic and fully computer-controlled instrument, so that very few human interventions are required from the winter-over crew. The instrument was improved continuously, to reduce these interventions as much as possible and to increase its performances. Data analysis were performed by using a pipeline implementations of the classical aperture photometry routines, for a daily automatic on-site data processing, and the Optimal Image Subtraction method on transferred data, in France, for more accurate processing.

During the first three years (2010-2012) of operation of the instrument, we observed 21 stellar fields; each field being observed continuously, during ~7 to ~30 days, from March to the end of September for each campaign. More than 200 000 frames were recorded and 310 000 stars analysed. We acquired a total of 1959 h, 1889 h and 1997 h of science exposure frames, reaching a duty cycle of 65.51%, 63.15% and 66.77% for the 2010, 2011 and 2012 campaign respectively. The point-to-point RMS plots show that the photometric precision at the bright end of our magnitude range (R~12 mag) reaches ~2 mmag, while for the dim end (R=17 mag), the noise rises to ~20 mmag. Although we achieve very high photometric precision for the brightest stars, we are well above the photon limit. The RMS scatter in the binned data (over a transit-length time interval of ~2.5 h) is typically ~500 ppm for the brightest stars, far worse than the ~100 ppm that would be achieved if the noise were uncorrelated. The red component of the noise comes from the systematic errors that affect our data. A large part of these systematic errors are caused by the seeing variations at the ground level and by the rapid temperature fluctuations that are specific to the high Antarctic plateau. ASTEP 400, which is located at ~2 m above the ground level, is very sensitive to these fluctuations in winter. We conducted some specific tests to identify how the image quality of the telescope and thus the photometric data quality are affected by these fluctuations and identified some ways to improve the instrument. These improvements should equip any future telescope operating in Antarctica.

We performed a box least-square (BLS) period search on each lightcurve and selected 43 possible planetary transit candidates. Twenty of these candidates were observed using spectroscopic follow-up. We found 7 candidates, which present no RV variations within 2 km s^{-1}, or 5 km s^{-1}, as possible 'good' planetary transit candidates requiring future higher spectroscopic resolution observations to measure more accurate RVs to confirm these candidates are true exoplanet systems. On the other hand, 9 candidates were rejected as eclipsing binaries and 6 not yet followed-up candidates were selected as possible good planetary candidates according to their stellar density vs. transit depth relation. In addition, from this analysis, we detected more than 1 900 new variable stars that will be the subject of a forthcoming paper.

These results demonstrate the high potential of ASTEP 400, installed at Dome C in Antarctica, to obtain extremely accurate and near-continuous photometric observations and to monitoring several thousands of stars, searching for transiting exoplanets.

REFERENCES

Abe L. et al., 2013, A&A, 553, A49
Alard C., Lupton R. H., 1998, ApJ, 503, 325
Aristidi E., Agabi A., Vernin J., Azouit M., Martin F., Ziad A., Fossat E., 2003, A&A, 406, L19
Aristidi E. et al., 2005, A&A, 430, 739
Aristidi E. et al., 2009, A&A, 499, 955
Ashley M. C. B., Burton M. G., Calisse P. G., Phillips A., Storey J. W. V., 2005, Highlights of Astronomy, 13, 932
Bonner C. S. et al., 2010, PASP, 122, 1122
Crouzet N. et al., 2010, A&A, 511, A36
Crouzet N. et al., 2013, in IAU Symposium, Vol. 288, IAU Symposium, Burton M. G., Cui X., Tothill N. F. H., eds., pp. 226–230
Dempsey J. T., Storey J. W. V., Phillips A., 2005, PASA, 22, 91
Dopita M., Hart J., McGregor P., Oates P., Bloxham G., Jones D., 2007, Ap&SS, 310, 255
Dopita M. et al., 2010, Ap&SS, 327, 245
Fossat E., Aristidi E., Agabi A., Bondoux E., Challita Z., Jeanneaux F., Mékarnia D., 2010, A&A, 517, A69
Fruth T. et al., 2014, PASP, 126, 227
Giordano C., Vernin J., Chadid M., Aristidi E., Agabi A., Trinquet H., 2012, PASP, 124, 494
Kenyon S. L., Lawrence J. S., Ashley M. C. B., Storey J. W. V., Tokovinin A., Fossat E., 2006, PASP, 118, 924
Kenyon S. L., Storey J. W. V., 2006, PASP, 118, 489
Kovács G., Zucker S., Mazeh T., 2002, A&A, 391, 369
Lawrence J. S., Ashley M. C. B., Tokovinin A., Travouillon T., 2004, Nature, 431, 278
Mandel K., Agol E., 2002, ApJL, 580, L171
Mazeh T. et al., 2009, A&A, 506, 431
Miller J. P., Pennypacker C. R., White G. L., 2008, PASP, 120, 449
Montalto M. et al., 2007, A&A, 470, 1137
Moore A. et al., 2008, in Society of Photo-Optical Instrumentation Engineers (SPIE) Conference Series, Vol. 7012, Society of Photo-Optical Instrumentation Engineers (SPIE) Conference Series, p. 26
Mosser B., Aristidi E., 2007, PASP, 119, 127
Penev K. et al., 2013, AJ, 145, 5
Petenko I. et al., 2014, A&A, 568, A44
Pont F., Zucker S., Queloz D., 2006, MNRAS, 373, 231

Rupprecht G. et al., 2004, in Society of Photo-Optical Instrumentation Engineers (SPIE) Conference Series, Vol. 5492, Ground-based Instrumentation for Astronomy, Moorwood A. F. M., Iye M., eds., pp. 148–159

Strassmeier K. G. et al., 2008, A&A, 490, 287

Tamuz O., Mazeh T., Zucker S., 2005, MNRAS, 356, 1466

Tingley B., Bonomo A. S., Deeg H. J., 2011, ApJ, 726, 112
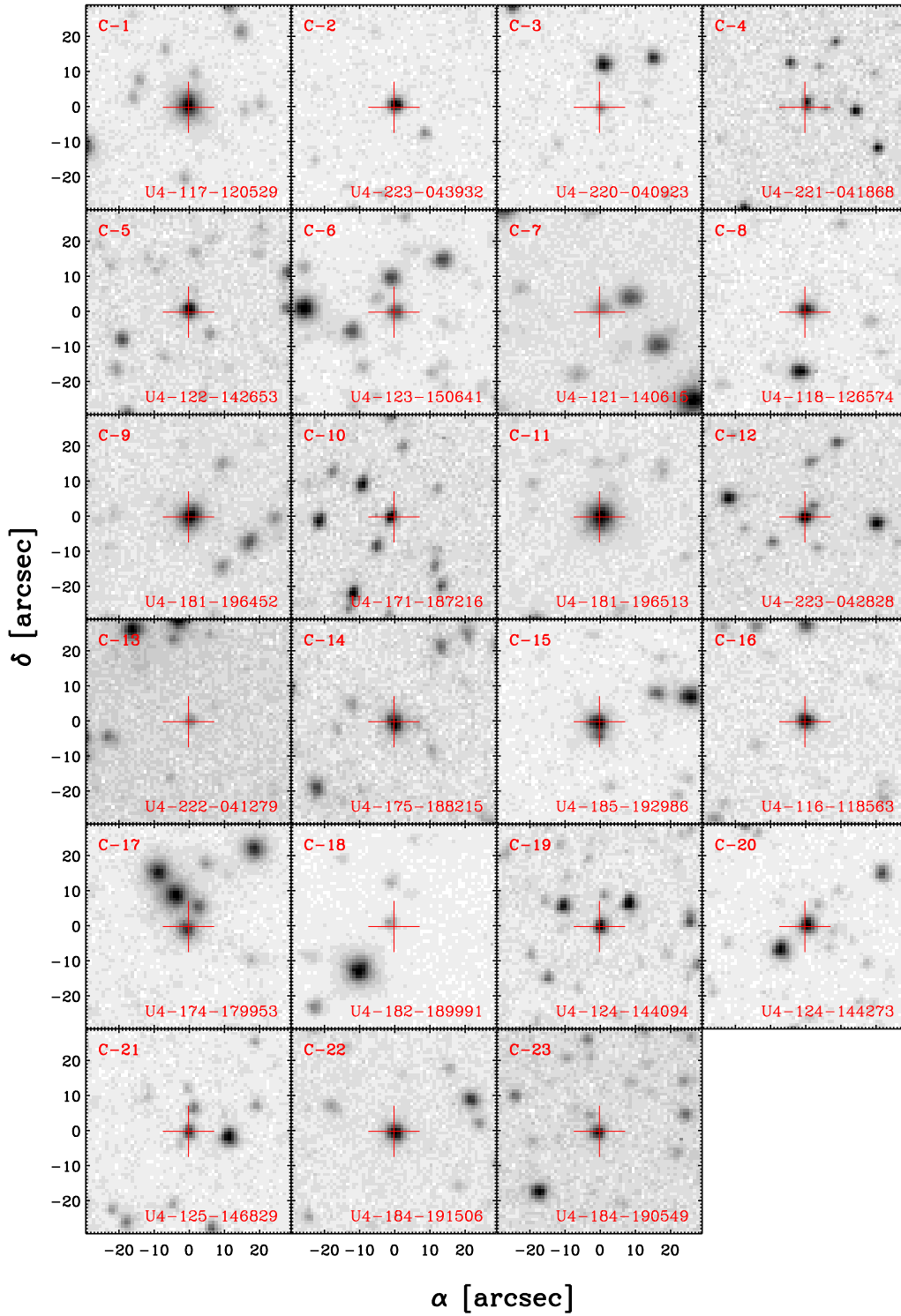
Wang L. et al., 2011, AJ, 142, 155

Figure 29. Zoom-in showing the neighborhood of candidates C-1 to C-23 on the sky. Sub-images (64 pixels × 64 pixels) are from ASTEP 400 reference frames of each stellar field. North is at top, East at left.
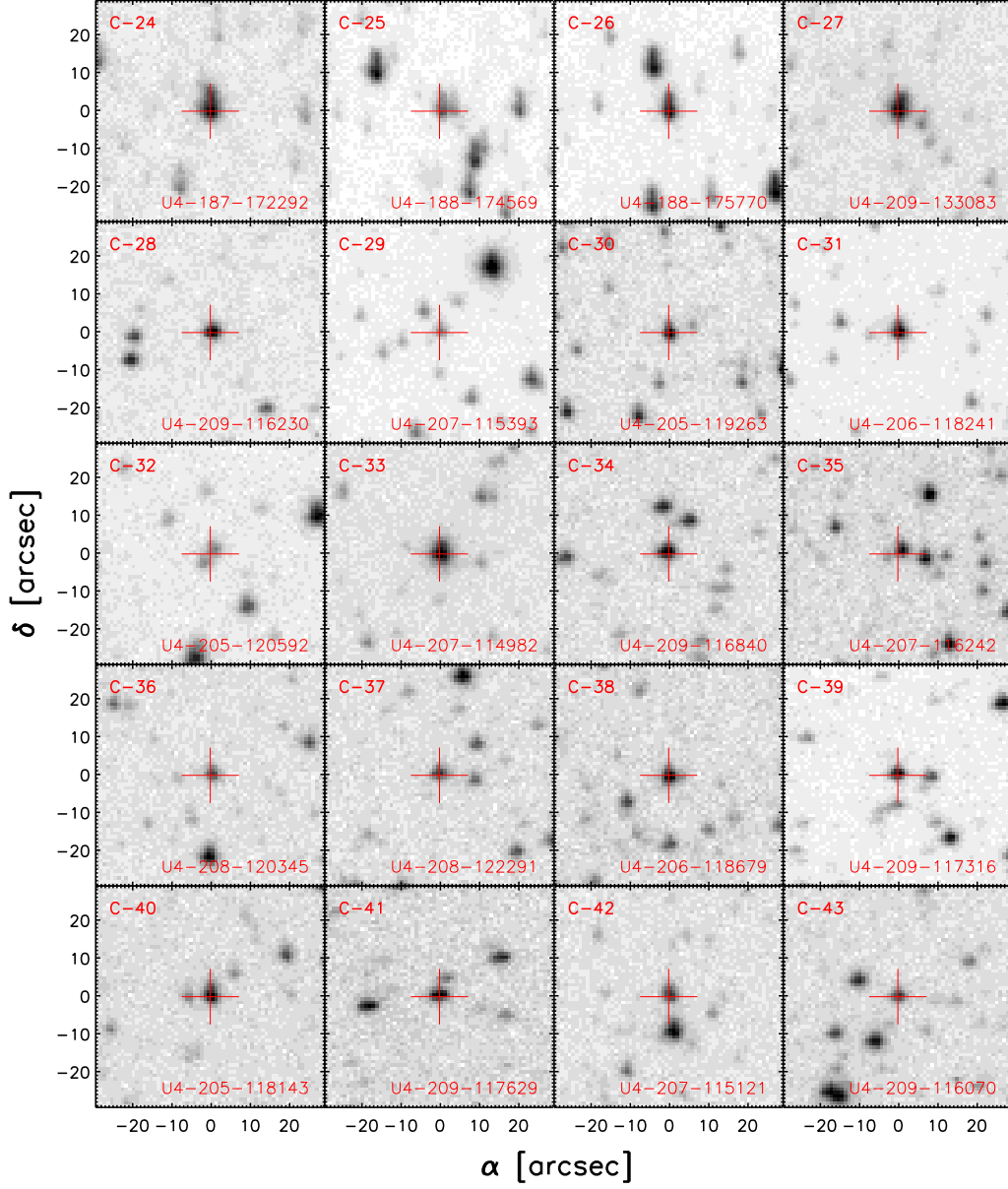
Figure 30. Zoom-in showing the neighborhood of candidates C-24 to C-43 on the sky. Sub-images (64 pixels × 64 pixels) are from ASTEP 400 reference frames of each stellar field. North is at top, East at left.